AFDM-Enabled Integrated Sensing and Communication: Theoretical Framework and Pilot Design

Fan Zhang, *Student Member, IEEE*, Zhaocheng Wang, *Fellow, IEEE*, Tianqi Mao, *Member, IEEE*,
Tianyu Jiao, Yinxiao Zhuo, Miaowen Wen, *Senior Member, IEEE*, Wei Xiang, *Senior Member, IEEE*,
Sheng Chen, *Life Fellow, IEEE*, and George K. Karagiannidis, *Fellow, IEEE*

Abstract—The integrated sensing and communication (ISAC) has been envisioned as one representative usage scenario of sixth-generation (6G) network. However, the unprecedented characteristics of 6G, especially the doubly dispersive channel, make classical ISAC waveforms rather challenging to guarantee a desirable performance level. The recently proposed affine frequency division multiplexing (AFDM) can attain full diversity even under doubly dispersive effects, thus becoming a competitive candidate for next-generation ISAC waveforms. Relevant investigations are still at an early stage, which involve only straightforward design lacking explicit theoretical analysis. This paper provides an in-depth investigation on AFDM waveform design for ISAC applications. Specifically, the closed-form Crámer-Rao bounds of target detection for AFDM are derived, followed by a demonstration on its merits over existing counterparts. Furthermore, we formulate the ambiguity function of the pilot-assisted AFDM waveform for the first time, revealing conditions for stable sensing performance. To further enhance both the communication and sensing performance of the AFDM waveform, we propose a novel pilot design by exploiting the characteristics of AFDM signals. The proposed design is analytically validated to be capable of optimizing the ambiguity function property and channel estimation accuracy simultaneously as well as overcoming the sensing and channel estimation range limitation originated from the pilot spacing. Numerical results have verified the superiority of the proposed pilot design in terms of dual-functional performance.

Fan Zhang, Zhaocheng Wang, Tianyu Jiao, and Yinxiao Zhuo are with the Department of Electronic Engineering, Tsinghua University, Beijing 100084, China (e-mail: zf22@mails.tsinghua.edu.cn; zcwang@tsinghua.edu.cn; jiaoty22@mails.tsinghua.edu.cn; zhuoyx20@mails.tsinghua.edu.cn).

Tianqi Mao is with the State Key Laboratory of Environment Characteristics and Effects for Near-Space, Beijing Institute of Technology, Beijing 100081, China, and also with Beijing Institute of Technology, Zhuhai 519088, China (e-mail: maotq@bit.edu.cn).

Miaowen Wen is with the School of Electronic and Information Engineering, South China University of Technology, Guangzhou 510006, China (e-mail: eemwwen@scut.edu.cn).

Wei Xiang is with the School of Computing Engineering and Mathematical Sciences, La Trobe University, Melbourne, VIC 3086, Australia (e-mail: w.xiang@latrobe.edu.au).

Sheng Chen is with the School of Computer Science and Technology, Ocean University of China, Qingdao 266100, China (e-mail: sqc@ecs.soton.ac.uk).

George K. Karagiannidis is with the Department of Electrical and Computer Engineering, Aristotle University of Thessaloniki, 541 24 Thessaloniki, Greece (e-mail: geokarag@auth.gr).

Digital Object Identifier 10.1109/JSAC.2025.3609766

I. INTRODUCTION

TO SUPPORT a plethora of emerging applications, such as autonomous driving, Internet of Things (IoT), and low-altitude economy, next-generation wireless networks are expected to not only maintain high-speed connectivity but also achieve reliable and high-resolution sensing capabilities [1], [2], [3]. To enable radar sensing with existing infrastructure of wireless communication networks, the integrated sensing and communication (ISAC) philosophy has been proposed as a promising solution for the sixth-generation (6G) networks [4], [5]. By sharing identical hardware and spectrum resources for both communication and sensing purposes, ISAC technology can realize dual functions simultaneously with desirable performance trade-off and efficient resource usage [6], [7], [8]. Furthermore, it can facilitate information exchange between sensing and communication modules, thereby further improving the performance of dual functions [9], [10], [11].

The integrated waveform design that optimally balances both communication and sensing performance is a core challenge in ISAC systems [12], [13]. Orthogonal frequency division multiplexing (OFDM), which is adopted in most commercial communication standards, has been extensively investigated within the context of ISAC waveform design [14], [15], [16]. Specifically, OFDM allows for flexible allocation of orthogonal resource elements (REs) between communication and sensing without mutual interference to achieve a good performance trade-off in time invariant channels [17]. However, in the doubly dispersive channel, which is prevalent when employing millimeter-wave/Terahertz frequencies under high mobility, OFDM suffers from notorious inter-carrier interference (ICI), causing communication performance degradation [18]. Furthermore, the destroyed subcarrier orthogonality incurs substantial mutual interference between communication and sensing, further impairing the performance of both functions.

To address this issue, several novel waveforms have been developed to ensure superior ISAC performance [19], [20], [21], [22]. The work [21] designed the multicarrier orthogonal chirp division multiplexing (OCDM) by using a series of chirp signals, which can achieve full diversity in frequency-selective channels, thereby showing better gain over OFDM [22]. However, this scheme fails to sufficiently exploit the diversity

gain in doubly dispersive channels, and it is fragile to fast time variations. Orthogonal time frequency space (OTFS) [19], which is a two-dimensional modulation technique that modulates communication symbols in the delay-Doppler domain, takes advantage of the diversity of both time and frequency shifts caused by high mobility, to ensure robust communication and sensing performance in doubly dispersive channels. Nevertheless, the large pilot overhead and the complex transceiver algorithms hinder OTFS from practical implementation.

Recently, affine frequency division multiplexing (AFDM) was proposed as a generalized form of OFDM and OCDM [23]. AFDM is based on the discrete affine Fourier transform (DAFT), and the parameters of DAFT can be optimized according to channel characteristics to achieve full diversity gain under doubly dispersive channels. Compared to existing waveforms, AFDM can deliver superior communication performance under high mobility scenarios with reduced complexity and channel estimation overhead, making it a promising candidate for next-generation ISAC applications.

A. Related Works on AFDM-Enabled ISAC

Conventional OFDM-based waveform designs are typically developed under the assumption of small Doppler shifts, where inter-carrier interference is negligible. This allows orthogonal resource elements to be allocated to communication and sensing functions separately, thereby avoiding mutual interference. In contrast, AFDM inherently exhibits coupling effect among subcarriers. The multipath propagation causes the energy of one subcarrier to spread across others, making it difficult to isolate the symbol carried by each subcarrier. As a result, conventional OFDM-based waveform design methodologies are no longer feasible in AFDM systems.

Compared to OFDM, the AFDM waveform has two adjustable parameters, c_1 and c_2, which increase the flexibility of ISAC waveform design. Specifically, the impact of c_1 on the bit error rate (BER) and the Crámer-Rao bound (CRB) of target ranging was investigated in [24], and an adaptive waveform design method was proposed to achieve different communication and sensing requirements by flexible adjustment of c_1. However, this study only offers numerical results and lacked theoretical analysis to support its conclusions. The work [25] derived a simplified form of the AFDM ambiguity function. Based on this derivation, a parameter selection criterion was proposed to optimize the delay estimation resolution without considering the Doppler shift aspect.

The study [26] proposed an AFDM-enabled ISAC system and designed two algorithms for target distance and velocity estimation in the time and DAFT domains, respectively. This system design employs entirely random communication symbols for sensing purpose, which fails to guarantee a stable sensing performance. To tackle this issue, a pilot-assisted ISAC scheme was presented in [27], where one single pilot symbol was utilized for target sensing rather than the whole frame. In addition, a low-complexity self-interference cancellation method was proposed to improve the estimation accuracy. However, to avoid mutual interference, a sufficient number of zero-padded guard subcarriers have to be inserted between the pilot and data, which wastes spectrum resources.

To enhance spectral efficiency, the superimposed pilot philosophy was proposed in [28], where pilots and data symbols are superimposed together to activate all subcarriers for transmission. However, the pilot spacing strongly depends on the maximum channel delay, and estimation performance is poor for channels with large delay spread. The sensing range of this design is also limited by the pilot spacing, making it difficult to satisfy the requirement of a large sensing range.

B. Motivation and Our Contributions

It can be seen from the above literature review that investigations on AFDM-enabled ISAC are still at a nascent stage, especially lacking theoretical analysis for its sensing performance. Existing AFDM-enabled ISAC waveforms struggle to balance the spectral efficiency, channel estimation accuracy and sensing capability simultaneously. Against this background, for the first time we derive the CRBs of distance and velocity estimation for AFDM-enabled sensing, along with the two-dimensional ambiguity function, thereby refining the theoretical framework for AFDM-enabled ISAC systems. Furthermore, by considering the superimposed pilot architecture, we propose a novel pilot design to optimize the ambiguity function property and the channel estimation performance simultaneously. The main contributions of this paper are summarized as follows.

1) To evaluate the sensing capability of AFDM-enabled ISAC waveform, closed-form CRB expressions for the distance and velocity estimation are derived. These results are applicable to other state-of-the-art multi-carrier waveforms that are special cases of AFDM, i.e., OFDM and OCDM, by setting $c_1 = 0$ and $c_1 = 1/2N$, respectively, where N is the number of DAFT points. Based on the derived CRBs and numerical analysis, we highlight the significant advantages of AFDM over existing counterparts, in terms of ISAC applications.

2) We present the formulation of the ambiguity function for the pilot-assisted AFDM waveform and analyze its statistical properties. Through theoretical analysis, we derive two conditions that can minimize the variance of the ambiguity function to realize stable sensing performance, which offer inspiring guidelines for AFDM-enabled ISAC system design.

3) To further enhance the dual-functional performance of the pilot-assisted AFDM waveform, a novel pilot design is proposed, which incorporates the parameter c_1 setting, the pilot spacing configuration and the pilot sequence design. The pilot sequence is designed to achieve an ideal ambiguity function by leveraging the unique multipath separation characteristics of AFDM based on the constant amplitude zero autocorrelation (CAZAC) sequences. The proposed design is validated theoretically to realize minimal channel estimation error. More importantly, it can overcome the limitations on maximum sensing range and delay spread imposed by the pilot spacing, and exhibits good dual-functional performance under large propagation delays.

4) Numerical results are offered to validate the superiority of the proposed pilot design in terms of communication
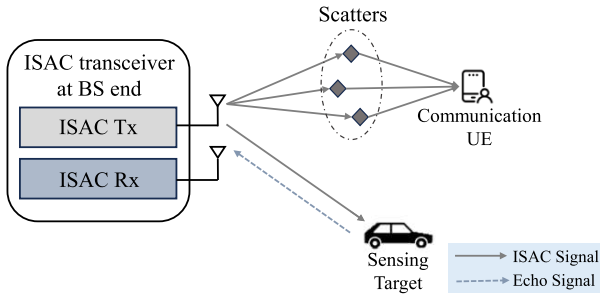
Fig. 1. Typical monostatic ISAC scenario.

and sensing performance. Compared to existing pilot schemes, our pilot design provides more accurate channel estimation, resulting in a lower BER at the same signal-to-noise ratio (SNR). Furthermore, owing to its ideal ambiguity function, our pilot design does not introduce high sidelobe interference in the target sensing, significantly reducing the false alarm probability and leading to a preferable receiver operating characteristic (ROC) curve. Simulations also show that the velocity and distance estimation errors of the proposed design are close to the derived CRBs.

C. Organization and Notations

The remainder of this paper is organized as follows. Section II introduces the AFDM-enabled ISAC system model. Section III presents our theoretical framework for AFDM-enabled ISAC by deriving the sensing CRBs and the ambiguity function of the pilot-assisted AFDM waveform. In Section IV, a novel pilot design is proposed to enhance the dual-functional performance. Numerical results are provided in Section V, followed by concluding remarks drawn in Section VI.

Notation: The m-th element of vector $\mathbf{x}$ is denoted by $x[m]$, while $X[m,k]$ denotes the element in the m-th row and the k-th column of matrix $\mathbf{X}$. $(\cdot)^*$, $(\cdot)^{\mathrm{T}}$, and $(\cdot)^{\mathrm{H}}$ denote the conjugate, transpose, and Hermitian operations, respectively. $\mathbf{I}_N$ denotes the $N \times N$ identity matrix. $\mathbf{x} \sim \mathcal{CN}(\mathbf{0}, \sigma^2 \mathbf{I}_N)$ represents that each element of $\mathbf{x} \in \mathbb{C}^{N \times 1}$ follows a complex Gaussian distribution with mean 0 and variance σ^2. The operator $\mathrm{diag}(\mathbf{x})$ transforms vector $\mathbf{x}$ into a diagonal matrix. $\|\mathbf{X}\|$ denotes the Frobenius norm of matrix $\mathbf{X}$. $\lfloor \cdot \rfloor$ is the floor function that rounds a real number to the nearest integer less than or equal to that number. $|\cdot|$ denotes the modulus operation. $\mathbb{E}\{\cdot\}$ denotes the expectation operation. $\langle \cdot \rangle_N$ denotes the modulo operation with divisor N. $\Re\{\cdot\}$ denotes the real part of a complex number.

II. SYSTEM MODEL

We consider a typical monostatic ISAC scenario as illustrated in Fig. 1, where the base station (BS) simultaneously transmits data to user equipment (UE) while leveraging the received echo signals to detect the presence of targets in the surrounding environment. The communication channel refers to the direct link between the BS and the UE, which consists of multiple clustered paths formed by scatterers between the base station and the user. The sensing channel represents the target reflection path observed at the BS, which is composed of

reflection paths generated by the target. These two channels are independent and uncorrelated in our considered model. Additionally, when a target is detected, the BS estimates its distance and relative radial velocity. Perfect cancellation of the resultant self-interference is assumed with sufficient isolation between the ISAC transmitter (Tx) and receiver (Rx), achieved by active radio-frequency cancellation methods or other related techniques [29].

A. Signal Model

The superimposed pilot scheme [28] is considered for the AFDM-enabled ISAC system owing to its high spectral efficiency. The N_c-length transmit vector in the DAFT domain is expressed as the superposition of the pilot and data parts:

$$\mathbf{x} = \mathbf{x}_{\mathrm{p}} + \mathbf{x}_{\mathrm{d}}, \tag{1}$$

where $\mathbf{x}_{\mathrm{p}} \in \mathbb{C}^{N_c \times 1}$ and $\mathbf{x}_{\mathrm{d}} \in \mathbb{C}^{N_c \times 1}$ denote the pilot and data signals, respectively. The pilot signal is deterministic with power $\sigma_{\mathrm{p}}^2 = \mathbf{x}_{\mathrm{p}}^{\mathrm{H}} \mathbf{x}_{\mathrm{p}}$, while the data counterpart is stochastic with $\mathbb{E}\{\mathbf{x}_{\mathrm{d}} \mathbf{x}_{\mathrm{d}}^{\mathrm{H}}\} = \sigma_{\mathrm{d}}^2 \mathbf{I}_{N_c}$. The overall signal power is given by

$$P_{\mathrm{t}} = \sigma_{\mathrm{p}}^2 + N_c \sigma_{\mathrm{d}}^2. \tag{2}$$

By performing the inverse DAFT on $\mathbf{x}$, the transmit signal in the time domain can be written as [30]

$$s[n] = \frac{1}{\sqrt{N_c}} \sum_{m=0}^{N_c-1} x[m] e^{j2\pi \eta_m[n]}, \ n = 0, \cdots, N_c - 1, \tag{3}$$

with

$$\eta_m[n] = c_1 n^2 + \frac{1}{N_c} mn + c_2 m^2, \tag{4}$$

where c_1 and c_2 are the DAFT parameters. To guarantee the optimal diversity order for AFDM, c_2 should be an irrational number, and c_1 should satisfy

$$\frac{2\nu_{\mathrm{m}} + 1}{2N_c} \le c_1 \le \frac{N_c}{2N_c(\tau_{\mathrm{m}} + 1)}, \tag{5}$$

where τ_{m} and ν_{m} denote the maximum normalized delay and Doppler shift, respectively. The lower bound is set to ensure that the effective channels corresponding to different paths do not overlap in the DAFT domain, while the upper bound is introduced to constrain the range of the maximum delay to avoid ambiguity in the DAFT representation of the effective channel. The process in (3) can be written in matrix form as

$$\mathbf{s} = \mathbf{\Lambda}_{c_2}^{\mathrm{H}} \mathbf{F}^{\mathrm{H}} \mathbf{\Lambda}_{c_1}^{\mathrm{H}} \mathbf{x} \triangleq \mathbf{A}^{\mathrm{H}} \mathbf{x}, \tag{6}$$

where $\mathbf{s} = [s[0], s[1], \cdots, s[N_c - 1]]^{\mathrm{T}} \in \mathbb{C}^{N_c \times 1}$, $\mathbf{F}$ is the N_c-point discrete Fourier transform (DFT) matrix, and $\mathbf{\Lambda}_{c_i} = \mathrm{diag}\left(\left[1, e^{j2\pi c_i}, \cdots, e^{j2\pi c_i (N_c-1)^2} \right]^{\mathrm{T}} \right) \in \mathbb{C}^{N_c \times N_c}$, while $\mathbf{A} = \mathbf{\Lambda}_{c_1} \mathbf{F} \mathbf{\Lambda}_{c_2} \in \mathbb{C}^{N_c \times N_c}$.

To combat the inter-symbol interference (ISI) incurred by multipath propagation, a chirp-periodic prefix (CPP) is inserted in front of each AFDM symbol. The length of the CPP, denoted as N_{cp}, is chosen to be larger than both the maximum integer delay of the communication channel and the maximum
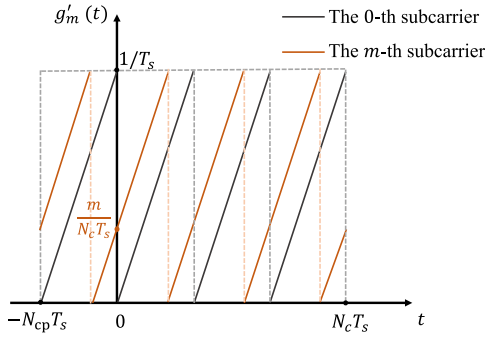
Fig. 2. The frequency of the AFDM subcarriers with respect to time.

integer round trip delay of the sensing target. According to the periodicity of AFDM, the CPP can be expressed as

$$s[n] = s[N_c + n]e^{-j2\pi c_1(N_c^2 + 2N_c n)}, \quad n = -N_{\mathrm{cp}}, \cdots, -1. \quad (7)$$

After adding the CPP, the discrete signals are fed into a digital-to-analog converter (D/A) to obtain the continuous transmit signal as

$$s(t) = \frac{1}{\sqrt{N_c}} \sum_{m=0}^{N_c-1} x[m] e^{j2\pi \left(g_m(t-N_{\mathrm{cp}}T_s) + c_2 m^2\right)}, \quad (8)$$

where $t \in \left[0, \ (N_c + N_{\mathrm{cp}}) T_s\right)$ and T_s is the sampling period, while $g_m(t)$ represents the instantaneous phase of the m-th subcarrier, and its derivative $g_m'(t)$ represents the instantaneous frequency as illustrated in Fig. 2. Due to the frequency wrapping property of AFDM chirp subcarriers, $g_m(t)$ can be expressed as

$$g_m(t) = c_1 \left(\frac{t}{T_s}\right)^2 + \frac{t}{N_c T_s} m - q_m \left(\frac{t}{T_s}\right) \frac{t}{T_s}, \quad (9)$$

where $q_m \left(\frac{t}{T_s}\right) = \left\lfloor 2c_1 \frac{t}{T_s} + \frac{m}{N_c} \right\rfloor$.

B. Channel Estimation and Data Demodulation

The multi-path time-varying communication channel is considered. By denoting the complex gain, delay and Doppler shift of the i-th path as α_i, μ_i and f_i, respectively, the channel coefficient of the i-th path can be expressed as

$$h_i(t, \mu) = \alpha_i e^{j2\pi f_i t} \delta(\mu - \mu_i). \quad (10)$$

After the analog-to-digital conversion, discarding CPP and performing N_c-point DAFT, the effective channel matrix of the i-th path in the DAFT domain can be written as [23]

$$\mathbf{H}_i = \alpha_i \mathbf{A} \mathbf{\Gamma}_{\mathrm{CPP}_i} \mathbf{\Pi}^{\tau_i} \mathbf{\Delta}_{\nu_i} \mathbf{A}^{\mathrm{H}}, \quad (11)$$

where $\tau_i = \lfloor \mu_i / T_s \rfloor \in [0, \tau_{\mathrm{m}}]$ denotes the normalized delay and $\nu_i = f_i N_c T_s = f_i / \Delta f \in [-\nu_{\mathrm{m}}, \nu_{\mathrm{m}}]$ denotes the normalized Doppler shift, while $\Delta f = 1 / N_c T_s$ is the subcarrier spacing. Besides, $\mathbf{\Gamma}_{\mathrm{CPP}_i} \in \mathbb{C}^{N_c \times N_c}$ is the CPP matrix given by

$$\mathbf{\Gamma}_{\mathrm{CPP}_i} = \mathrm{diag}\left(\begin{cases} e^{-j2\pi c_1(N_c^2 + 2N_c(n - \tau_i))}, & n < \tau_i, \\ 1, & n \geq \tau_i, \end{cases}\right), \quad (12)$$

where n is the index of the diagonal elements, $\mathbf{\Pi}$ is the forward cyclic-shift matrix written as

$$\mathbf{\Pi} = \begin{bmatrix} 0 & \cdots & 0 & 1 \\ 1 & \cdots & 0 & 0 \\ \vdots & \ddots & \vdots & \vdots \\ 0 & \cdots & 1 & 0 \end{bmatrix}, \quad (13)$$

and $\mathbf{\Delta}_{\nu_i} = \mathrm{diag}\left(1, e^{j2\pi\nu_i/N_c}, \cdots, e^{j2\pi\nu_i(N_c-1)/N_c}\right)$ stands for the Doppler shift matrix.

Since the channel matrix for the path with a fractional normalized Doppler shift can be represented as a linear combination of matrices for paths with integer normalized Doppler shift, we use all integer Doppler paths as the basis to express the communication channel. Considering the maximum delay and Doppler shift, there are at most $L_{\mathrm{m}} = (2\nu_{\mathrm{m}} + 1)(\tau_{\mathrm{m}} + 1)$ paths. Therefore, the received signal $\mathbf{y} \in \mathbb{C}^{N_c \times 1}$ in the DAFT domain can be expressed as

$$\mathbf{y} = \mathbf{H}_{\mathrm{eff}} \mathbf{x} + \mathbf{w}_c = \sum_{i=1}^{L_{\mathrm{m}}} \mathbf{H}_i \mathbf{x} + \mathbf{w}_c$$

$$= \sum_{i=1}^{L_{\mathrm{m}}} \alpha_i \mathbf{\Phi}_i (\mathbf{x}_{\mathrm{p}} + \mathbf{x}_{\mathrm{d}}) + \mathbf{w}_c, \quad (14)$$

where $\mathbf{w}_c \sim \mathcal{CN}(\mathbf{0}, \sigma_{\mathrm{cn}}^2 \mathbf{I}_N)$ represents the noise, and $\mathbf{\Phi}_i = \mathbf{A} \mathbf{\Gamma}_{\mathrm{CPP}_i} \mathbf{\Pi}^{\tau_i} \mathbf{\Delta}_{\nu_i} \mathbf{A}^{\mathrm{H}}$ with τ_i and ν_i given by

$$\tau_i = \left\lfloor \frac{i-1}{2\nu_{\mathrm{m}} + 1} \right\rfloor, \quad (15)$$

$$\nu_i = \langle i - 1 \rangle_{2\nu_{\mathrm{m}}+1} - \nu_{\mathrm{m}}. \quad (16)$$

To estimate the effective channel $\mathbf{H}_{\mathrm{eff}}$, we employ the pilot signal to obtain the complex gain of each possible path. By denoting $\boldsymbol{\alpha} = \left[\alpha_1, \alpha_2, \cdots, \alpha_{L_{\mathrm{m}}}\right]^{\mathrm{T}}$, (14) can be rewritten as

$$\mathbf{y} = \left(\mathbf{\Psi}_{\mathrm{p}} + \mathbf{\Psi}_{\mathrm{d}}\right) \boldsymbol{\alpha} + \mathbf{w}_c = \mathbf{\Psi}_{\mathrm{p}} \boldsymbol{\alpha} + \hat{\mathbf{w}}, \quad (17)$$

where $\mathbf{\Psi}_{\mathrm{p}} = \left[\mathbf{\Phi}_1 \mathbf{x}_{\mathrm{p}}, \mathbf{\Phi}_2 \mathbf{x}_{\mathrm{p}}, \cdots, \mathbf{\Phi}_{L_{\mathrm{m}}} \mathbf{x}_{\mathrm{p}}\right] \in \mathbb{C}^{N_c \times L_{\mathrm{m}}}$ and $\mathbf{\Psi}_{\mathrm{d}} = \left[\mathbf{\Phi}_1 \mathbf{x}_{\mathrm{d}}, \mathbf{\Phi}_2 \mathbf{x}_{\mathrm{d}}, \cdots, \mathbf{\Phi}_{\mathbf{L}_{\mathrm{m}}} \mathbf{x}_{\mathrm{d}}\right] \in \mathbb{C}^{N_c \times L_{\mathrm{m}}}$, while $\hat{\mathbf{w}} \triangleq \mathbf{\Psi}_{\mathrm{d}} \boldsymbol{\alpha} + \mathbf{w}_c$ defines the effective noise with the covariance matrix $\mathbf{C}_{\hat{\mathbf{w}}}$. Using the minimum mean square error (MMSE) algorithm yields the estimated complex gain vector:

$$\hat{\boldsymbol{\alpha}} = \left(\mathbf{\Psi}_{\mathrm{p}}^{\mathrm{H}} \mathbf{C}_{\hat{\mathbf{w}}}^{-1} \mathbf{\Psi}_{\mathrm{p}} + \mathbf{C}_{\boldsymbol{\alpha}}^{-1}\right)^{-1} \mathbf{\Psi}_{\mathrm{p}}^{\mathrm{H}} \mathbf{C}_{\hat{\mathbf{w}}}^{-1} \mathbf{y}, \quad (18)$$

where $\mathbf{C}_{\boldsymbol{\alpha}} = E\{\boldsymbol{\alpha} \boldsymbol{\alpha}^{\mathrm{H}}\} = \mathrm{diag}\left(\left[\sigma_{\alpha_1}^2, \sigma_{\alpha_2}^2, \cdots, \sigma_{\alpha_{L_{\mathrm{m}}}}^2\right]^{\mathrm{T}}\right)$ is the covariance matrix of $\boldsymbol{\alpha}$. We define a path indicator vector $\mathbf{b} = \left[b_1, b_2, \cdots, b_{L_{\mathrm{m}}}\right]^{\mathrm{T}}$, where b_i indicates whether the i-th path exists or not, i.e.,

$$b_i = \begin{cases} 1, & \text{if, } \hat{\alpha}_i > \epsilon, \\ 0, & \text{otherwise,} \end{cases} \quad (19)$$

in which ϵ is a predefined threshold. Then the estimated effective channel is given by

$$\hat{\mathbf{H}}_{\mathrm{eff}} = \sum_{i=1}^{L_{\mathrm{m}}} b_i \hat{\alpha}_i \mathbf{\Phi}_i. \quad (20)$$

The communication data are demodulated using the estimated channel. The channel estimation and data demodulation can be
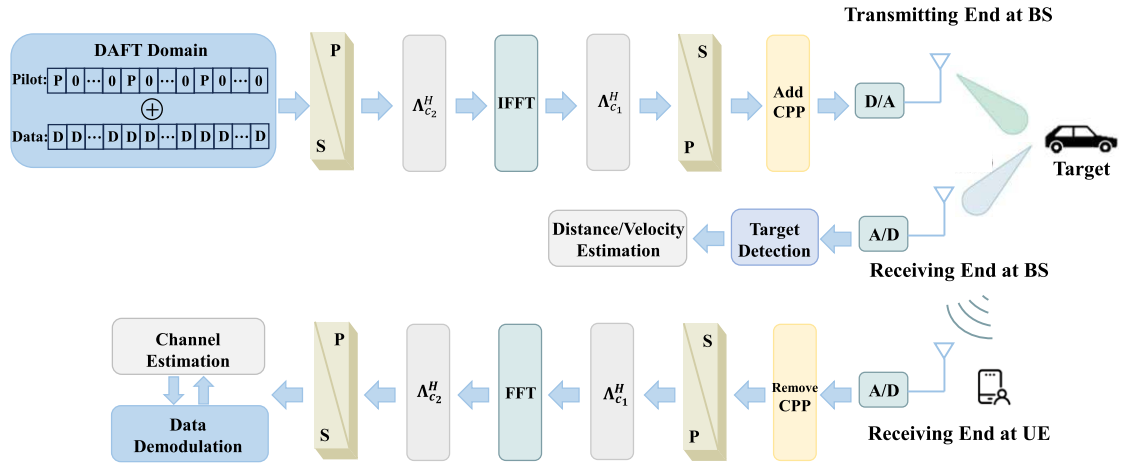
Fig. 3. Transceiver model of the AFDM-enabled ISAC system, where the signal reflected by the target is received by the receiving end at the BS for sensing purposes, and the signal through the downlink communication channel is received by the receiving end at the UE.

iteratively operated to reduce the mutual interference between the data and pilot signals, thereby enhancing the channel estimation accuracy and data detection performance [28].

C. Target Sensing

Assume that the transmit signal is reflected by a point target with the distance R and relative radial velocity V. The received echoes at the BS can be expressed as

$$r_\mathrm{s}(t) = \beta s(t - \bar{\mu})e^{j2\pi \bar{f}t} + w_\mathrm{s}(t), \tag{21}$$

where $\bar{\mu} = \frac{2R}{c}$ and $\bar{f} = \frac{2Vf_c}{c}$ with f_c and c being the carrier frequency and the speed of light, respectively, β is the complex gain, and $w_\mathrm{s}(t) \sim \mathcal{CN}(0, \sigma_\mathrm{s}^2)$ denotes the thermal noise plus the clutters. After passing through the analog-to-digital converter, the received signal is sampled with the period T_s, yielding

$$r_\mathrm{s}[n] = r_\mathrm{s}(nT_s) = \beta s(nT_s - \bar{\mu})e^{j2\pi\bar{\nu}n/N_c} + w_\mathrm{s}[nT_s], \tag{22}$$

where $\bar{\nu} = \bar{f}/\Delta f$ is the normalized Doppler shift. After the CPP removal, the target sensing can be performed using detection algorithms, such as cyclic correlation method [31], 2D-FFT [32] or MUSIC schemes [33]. To simultaneously obtain the distance and velocity information of the target, we consider a Doppler compensation-based correlation method, which yields the range-Doppler function (RDF) written as

$$E(\tau, \nu) = \sum_{n=0}^{N_c-1} r_\mathrm{s}^*[n]s[n - \tau]e^{j2\pi\nu n/N_c}, \tag{23}$$

where $\tau \in [0, \tau_\mathrm{m}]$ is the index of the correlation function and $\nu \in [-\nu_\mathrm{m}, \nu_\mathrm{m}]$ is the normalized frequency offset for Doppler compensation. Based on the RDF, the target can be detected via the hypothesis test. Let the test threshold be γ. The hypothesis can be expressed as

$$\mathrm{H}_1 : \frac{|E(\tau, \nu)|^2}{N(\tau, \nu)} > \gamma, \quad \mathrm{H}_0 : \frac{|E(\tau, \nu)|^2}{N(\tau, \nu)} < \gamma, \tag{24}$$

where H_1 and H_0 represent the presence and absence of the target, respectively, $N(\tau, \nu)$ denotes the average noise power at point (τ, ν), which can be calculated by averaging $|E(\tau, \nu)|^2$ in the whole or local region in the delay-Doppler domain [34].

If the hypothesis H_1 holds true at point $(\hat{\tau}, \hat{\nu})$, i.e., $(\hat{\tau}, \hat{\nu})$ corresponds to a target, then the distance and velocity of the target can be derived as

$$\hat{R} = \frac{c\hat{\tau}T_s}{2}, \quad \hat{\tau} = [0, \Delta\tau, 2\Delta\tau, \cdots, \tau_\mathrm{m}], \tag{25}$$

$$\hat{V} = \frac{c\hat{\nu}\Delta f}{2f_\mathrm{c}}, \quad \hat{\nu} = [-\nu_\mathrm{m}, \cdots, -\Delta\nu, 0, \Delta\nu, \cdots, \nu_\mathrm{m}], \tag{26}$$

where $\Delta\tau$ and $\Delta\nu$, are the resolutions for delay and Doppler shift estimations, respectively. According to (23), $\Delta\tau$ can be reduced by oversampling $r_\mathrm{s}[n]$ and $s[n]$, and $\Delta\nu$ can be reduced with a finer-grained Doppler shift compensation.

III. THEORETICAL FRAMEWORK FOR AFDM-ENABLED ISAC

The schematic diagram of the transceiver for the proposed AFDM-enabled ISAC system is depicted in Fig. 3. To investigate the sensing capability of the AFDM waveform, we derive its CRBs for distance and velocity estimations, and analyze its advantage over classical OFDM and OCDM.

A. Sensing CRBs Analysis

Let $\boldsymbol{\theta} = [\beta, \bar{\tau}, \bar{v}]^\mathrm{T}$ be the unknown parameters for target sensing. According to (22), by denoting $\bar{s}[n] = \beta s(nT_s - \bar{\tau}T_s)e^{j2\pi\bar{\nu}n/N_c}$, the received echo signal in matrix form can be expressed as

$$\mathbf{r}_\mathrm{s} = \bar{\mathbf{s}} + \mathbf{w}_\mathrm{s}, \tag{27}$$

where $\bar{\mathbf{s}} = [\bar{s}[0], \cdots, \bar{s}[N_c-1]]^\mathrm{T}$, $\mathbf{r}_\mathrm{s} = [r_\mathrm{s}[0], \cdots, r_\mathrm{s}[N_c-1]]^\mathrm{T}$ and $\mathbf{w}_\mathrm{s} = [w_\mathrm{s}[0], \cdots, w_\mathrm{s}[N_c-1]]^\mathrm{T} \sim \mathcal{CN}(\mathbf{0}, \sigma_\mathrm{s}^2\mathbf{I}_{N_c})$. The log-likelihood function of $\mathbf{r}_\mathrm{s}$ with respect to $\boldsymbol{\theta}$ is defined by

$$\log p(\mathbf{r}_\mathrm{s}, \boldsymbol{\theta}) = -\frac{1}{\sigma_\mathrm{s}^2}(\mathbf{r}_\mathrm{s} - \bar{\mathbf{s}})^\mathrm{H}(\mathbf{r}_\mathrm{s} - \bar{\mathbf{s}}) - C_1, \tag{28}$$

where $C_1 = N_c \log(\sqrt{2\pi}\sigma_\mathrm{s})$ is a constant term. To obtain the Fisher information matrix (FIM), denoted as $\mathbf{F_I}$, we calculate the expectation of the partial derivatives of the log-likelihood function with respect to the elements of $\boldsymbol{\theta}$ as follows

$$F_I[i, j] = -\mathbb{E}\left\{ \frac{\partial^2 \log p(\mathbf{r}_\mathrm{s}, \boldsymbol{\theta})}{\partial \theta_i \partial \theta_j^*} \right\}$$

$$= \frac{2}{\sigma_s^2} \Re \left\{ \mathbb{E} \left\{ \left(\frac{\partial \bar{\mathbf{s}}}{\partial \theta_j} \right)^{\mathrm{H}} \left(\frac{\partial \bar{\mathbf{s}}}{\partial \theta_i} \right) \right\} \right\}$$

$$= \frac{2}{\sigma_s^2} \Re \left\{ \mathbb{E} \left\{ \sum_{n=0}^{N_c-1} \left(\frac{\partial \bar{s}[n]}{\partial \theta_j} \right)^* \left(\frac{\partial \bar{s}[n]}{\partial \theta_i} \right) \right\} \right\}, \quad (29)$$

where $\theta_i = \theta[i]$. The derivatives with respect to β, $\bar{\nu}$ and $\bar{\tau}$ can be deduced respectively as

$$\frac{\partial \bar{s}[n]}{\partial \beta} = s(nT_s - \bar{\tau}T_s)e^{j2\pi\bar{\nu}n/N_c}, \quad (30)$$

$$\frac{\partial \bar{s}[n]}{\partial \bar{\nu}} = \beta(j2\pi n/N_c)s(nT_s - \bar{\tau}T_s)e^{j2\pi\bar{\nu}n/N_c}, \quad (31)$$

$$\frac{\partial \bar{s}[n]}{\partial \bar{\tau}} \approx \frac{\beta e^{j2\pi\bar{\nu}n/N_c}}{\sqrt{N_c}} \sum_{m=0}^{N_c-1} \left(-j2\pi\mathcal{F}_m(n-\bar{\tau}) \right) x[m]$$
$$\times e^{j2\pi\left(g_m(nT_s-\bar{\tau}T_s)+c_2m^2\right)}, \quad (32)$$

where $\mathcal{F}_m(n-\bar{\tau}) = \left(2c_1(n-\bar{\tau}) + \frac{m}{N_c} \right) - \left\lfloor 2c_1(n-\bar{\tau}) + \frac{m}{N_c} \right\rfloor$ represents the fractional part of $2c_1(n-\bar{\tau}) + \frac{m}{N_c}$. The derivations of $\frac{\partial \bar{s}[n]}{\partial \beta}$ and $\frac{\partial \bar{s}[n]}{\partial \bar{\nu}}$ are straightforward. The derivation of $\frac{\partial \bar{s}[n]}{\partial \bar{\tau}}$ can be found in Appendix A.

Substituting (30)–(32) into (29) yields the approximate FIM for $\boldsymbol{\theta}$ (33), as shown at the bottom of the page where $P_m = \mathbb{E}\{|x[m]|^2\}$ is the allocated power on the m-th subcarrier and $P_t = \sum_{m=0}^{N_c-1} P_m$ is the total power of one AFDM symbol. The derivation of $\mathbf{F_I}$ is given in Appendix A.

The CRBs of $\bar{\tau}$ and $\bar{\nu}$, denoted as $\mathrm{CRB}_{\bar{\tau}}$ and $\mathrm{CRB}_{\bar{\nu}}$, can be derived by calculating the inverse of $\mathbf{F_I}$, which are given in (34) and (35), as shown at the bottom of the page, respectively. Specifically, by substituting $P_m = \mathbb{E}\{|x_d[m]|^2\}$ and $P_m = |x_p[m]|^2 + \mathbb{E}\{|x_d[m]|^2\}$ into the expression of sensing CRBs, we can obtain the sensing CRBs for full data ADFM signals and pilot-assisted AFDM signals, respectively. Accordingly, the CRBs of distance R and velocity V can be obtained as

$$\mathrm{CRB}_R = \left(\frac{cT_s}{2} \right)^2 \mathrm{CRB}_{\bar{\tau}}, \quad (36)$$

$$\mathrm{CRB}_V = \left(\frac{c\Delta f}{2f_c} \right)^2 \mathrm{CRB}_{\bar{\nu}}. \quad (37)$$

Fig. 4. Comparison the PDFs of $\mathrm{CRB}_{\bar{\tau}}$ for AFDM, OCDM and OFDM.

The above expressions for the CRBs are applicable not only to AFDM but also to OFDM and OCDM by choosing $c_1 = 0$ and $c_1 = \frac{1}{2N_c}$, respectively, in (36) and (37).

Based on the above results, we investigate the robustness of the sensing CRBs for different waveforms to dynamic subcarrier power allocation strategies during communications. We focus on $\mathrm{CRB}_{\bar{\tau}}$. A similar conclusion can be drawn for $\mathrm{CRB}_{\bar{\nu}}$ by using the same method, which therefore is omitted. To characterize the sensitivity of $\mathrm{CRB}_{\bar{\tau}}$ to the power variation of each subcarrier, we define the sensing weight of the m-th subcarrier as the partial derivative of $\mathrm{CRB}_{\bar{\tau}}$ with respect to P_m under equal power allocation, which is given by

$$\delta_m = \frac{\partial \mathrm{CRB}_{\bar{\tau}}}{\partial P_m} \bigg|_{(P_0,P_1,\cdots,P_{N_c-1})=\left(\frac{P_t}{N_c}, \frac{P_t}{N_c}, \cdots, \frac{P_t}{N_c} \right)}. \quad (38)$$

When the sensing weights of subcarriers are similar and close to zero, the importance of each subcarrier to target sensing becomes approximately equal. In this case, the impact of the subcarrier power allocation variation on the sensing performance can be considered negligible. Conversely, if the weights differ significantly among subcarriers, their importance to target sensing varies greatly, making the sensing performance more sensitive to the subcarrier power allocation strategy. The left section of Fig. 4 illustrates the subcarrier weights for AFDM ($c_1 = \frac{2\nu_m+1}{2N_c}$), OCDM ($c_1 = \frac{1}{2N_c}$) and OFDM ($c_1 = 0$), where the number of subcarriers is set to $N_c = 16$. It can be observed that AFDM achieves the most balanced subcarrier weights with values closest to 0, while OFDM

$$\mathbf{F_I} \approx \frac{2}{\sigma_s^2} \begin{bmatrix} \frac{P_t}{N_c} & 0 & 0 \\ 0 & \beta^2 \frac{(2\pi)^2}{N_c} \sum_n \sum_m P_m(\mathcal{F}_m(n-\bar{\tau}))^2 & \beta^2 \frac{(2\pi)^2}{N_c} \sum_n \sum_m P_m(-\mathcal{F}_m(n-\bar{\tau}))\left(\frac{n}{N_c} \right) \\ 0 & \beta^2 \frac{(2\pi)^2}{N_c} \sum_n \sum_m P_m(-\mathcal{F}_m(n-\bar{\tau}))\left(\frac{n}{N_c} \right) & \beta^2 \frac{(2\pi)^2}{N_c} \sum_n \sum_m P_m \left(\frac{n}{N_c} \right)^2 \end{bmatrix}. \quad (33)$$

$$\mathrm{CRB}_{\bar{\tau}} \approx \frac{\frac{\sigma_s^2 N_c}{8\pi^2\beta^2} \sum_n \sum_m P_m \left(\frac{n}{N_c} \right)^2}{\left(\sum_n \sum_m P_m(\mathcal{F}_m(n-\bar{\tau}))^2 \right) \left(\sum_n \sum_m P_m \left(\frac{n}{N_c} \right)^2 \right) - \left(\sum_n \sum_m P_m(\mathcal{F}_m(n-\bar{\tau}))\left(\frac{n}{N_c} \right) \right)^2}, \quad (34)$$
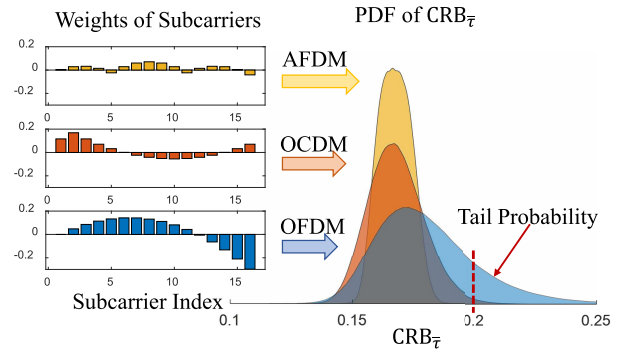
$$\mathrm{CRB}_{\bar{\nu}} \approx \frac{\frac{\sigma_s^2 N_c}{8\pi^2\beta^2} \sum_n \sum_m P_m(\mathcal{F}_m(n-\bar{\tau}))^2}{\left(\sum_n \sum_m P_m(\mathcal{F}_m(n-\bar{\tau}))^2 \right) \left(\sum_n \sum_m P_m \left(\frac{n}{N_c} \right)^2 \right) - \left(\sum_n \sum_m P_m(\mathcal{F}_m(n-\bar{\tau}))\left(\frac{n}{N_c} \right) \right)^2}. \quad (35)$$

exhibits the largest fluctuations in weight factors. This means that $\mathrm{CRB}_{\bar{\tau}}$ of AFDM maintains a relatively stable value even under significant variations in power allocation. Therefore, AFDM demonstrates more robust sensing performance in the scenarios with flexible power allocation, such as multi-user scenarios with dynamic demands.

To further explain the above conclusion, the right section of Fig. 4 presents the probability density function (PDF) of $\mathrm{CRB}_{\bar{\tau}}$. The PDF is obtained by calculating and statistically analyzing the values of $\mathrm{CRB}_{\bar{\tau}}$ under various random subcarrier power allocation strategies. It can be seen that although the mean values of $\mathrm{CRB}_{\bar{\tau}}$ for the three waveforms are similar, their variances differ significantly. OFDM exhibits the highest tail probability due to its largest variance, which increases the likelihood of degraded sensing performance. In contrast, AFDM has a negligible tail on the PDF curve, which makes it more likely to maintain the desired level of sensing performance.

B. Ambiguity Function Analysis

The CRB only provides a theoretical lower bound of sensing deviation. To explore the inherent characteristics of AFDM waveform in terms of both sensing and communication capabilities, we derive the ambiguity function of the pilot-assisted AFDM waveform and analyze its statistical properties.

Ambiguity function is defined as the two-dimensional correlation function in the delay-Doppler domain, which is essential for evaluating the sensing performance of various waveforms. Ambiguity functions can be classified into continuous and discrete ones, where the latter is considered as a sampled version of the former at integer points. For simplicity, this paper mainly investigates the discrete ambiguity function $\chi(\tau, \nu)$ of the N-length sequence $s(n)$, calculated as [35]

$$\chi(\tau, \nu) = \sum_{n=0}^{N-1} s^*[n]s[n - \tau]e^{j2\pi\nu n/N}, \quad (39)$$

where τ and ν denote the integer delay and Doppler indices, respectively. Since the CPP part only introduces a constant multiplicative factor in the derivation of ambiguity function, we omit it for brevity. Comparing (39) with (23), the RDF $E(\tau, \nu)$ is equivalent to $\chi(\tau, \nu)$ shifted by $(\bar{\tau}, \bar{\nu})$ and multiplied by a constant without consideration of noise. As we focus on the region $\Omega_{\mathrm{R}} = [0, \tau_{\mathrm{m}}] \times [-\nu_{\mathrm{m}}, \nu_{\mathrm{m}}]$ in the RDF, we only consider the region in $\chi(\tau, \nu)$ that can be shifted by $(\bar{\tau}, \bar{\nu})$ into the Ω_{R}, which can be expressed as $\Omega_{\mathrm{A}} = [-\tau_{\mathrm{m}}, \tau_{\mathrm{m}}] \times [-2\nu_{\mathrm{m}}, 2\nu_{\mathrm{m}}]$.

By taking the expression of a single AFDM symbol into (39), the ambiguity function can be derived as

$$\chi(\tau, \nu)$$
$$= \frac{1}{N_c} \sum_{n=0}^{N_c-1} \left(\sum_{m_1=0}^{N_c-1} x^*[m_1]e^{-j2\pi\left(c_1 n^2 + \frac{m_1 n}{N_c} + c_2 m_1^2\right)} \right)$$
$$\times \left(\sum_{m_2=0}^{N_c-1} x[m_2]e^{j2\pi\left(c_1(n-\tau)^2 + \frac{m_2(n-\tau)}{N_c} + c_2 m_2^2\right)} \right) e^{j2\pi\nu n/N_c}$$
$$= C_2 \sum_{m_1=0}^{N_c-1}\sum_{m_2=0}^{N_c-1} x^*[m_1]x[m_2]S^{(\tau,\nu)}(m_1, m_2)e^{-\frac{j2\pi m_2 \tau}{N_c}}, \quad (40)$$

where $C_2 = e^{j2\pi c_1 \tau^2}/N_c$, and $S^{(\tau,\nu)}(m_1, m_2)$ is the interference coefficient between the m_1-th and m_2-th subcarriers given by

$$S^{(\tau,\nu)}(m_1, m_2) \triangleq \sum_{n=0}^{N_c-1} e^{j2\pi\left(c_2(m_2^2 - m_1^2) - \left(2c_1\tau + \frac{m_1}{N_c} - \frac{m_2}{N_c} - \frac{\nu}{N_c}\right)n\right)}. \quad (41)$$

For simplicity, we assume that $2c_1 N_c$ is always an integer [23]. Then $S^{(\tau,\nu)}(m_1, m_2)$ can be further calculated as

$$S^{(\tau,\nu)}(m_1, m_2) = \begin{cases} N_c e^{j2\pi c_2(m_2^2 - m_1^2)}, & \text{if } \langle m_2 - m_1 \rangle_{N_c} = \mathrm{loc}^{(\tau,\nu)}, \\ 0, & \text{otherwise}, \end{cases} \quad (42)$$

where $\mathrm{loc}^{(\tau,\nu)} = 2c_1\tau N_c - \nu$ denotes the subcarrier offset incurred by τ and ν.

Based on the aforementioned results, several theorems are provided to reveal the statistical properties of the ambiguity function of the considered AFDM waveform.

Theorem 1: The ambiguity function of the pilot-assisted AFDM waveform can be expressed as

$$\chi(\tau, \nu)$$
$$= \chi_{\mathrm{p}}(\tau, \nu) + \chi_{\mathrm{d}}(\tau, \nu)$$
$$+ C_2 \left(\sum_{m_1=0}^{N_c-1}\sum_{m_2=0}^{N_c-1} x_d^*[m_1]x_p[m_2]e^{-j2\pi\frac{m_2\tau}{N_c}}S^{(\tau,\nu)}(m_1, m_2) \right.$$
$$\left. + \sum_{m_1=0}^{N_c-1}\sum_{m_2=0}^{N_c-1} x_p^*[m_1]x_d[m_2]e^{-j2\pi\frac{m_2\tau}{N_c}}S^{(\tau,\nu)}(m_1, m_2) \right), \quad (43)$$

where $\chi_{\mathrm{p}}(\tau, \nu)$ and $\chi_{\mathrm{d}}(\tau, \nu)$ are the ambiguity functions of pilot and data signals, respectively.

Proof: See Appendix B. □

For brevity, we denote the third and forth terms of (43) as $\chi_{\mathrm{dp}}(\tau, \nu)$ and $\chi_{\mathrm{pd}}(\tau, \nu)$, and thus $\chi(\tau, \nu)$ can be expressed as

$$\chi(\tau, \nu) = \chi_{\mathrm{p}}(\tau, \nu) + \chi_{\mathrm{d}}(\tau, \nu) + \chi_{\mathrm{dp}}(\tau, \nu) + \chi_{\mathrm{pd}}(\tau, \nu). \quad (44)$$

To derive the expectation and variance of $\chi(\tau, \nu)$, we first present the following assumptions.

1) The constellation diagrams considered have at least three distinct phase values, and all the constellation points are symmetrically distributed with respect to the center, leading to

$$\mathbb{E}\{x_d[m]\} = 0, \ m = 0, 1, \cdots, N_c - 1, \quad (45)$$
$$\mathbb{E}\{x_d^2[m]\} = 0, \ m = 0, 1, \cdots, N_c - 1. \quad (46)$$

Except for binary phase shift keying (BPSK), most common modulation formats, such as quadrature phase shift keying (QPSK) and 16-quadrature amplitude modulation (16-QAM), satisfy assumption 1.

2) The symbols modulated on different subcarriers are independent and identically distributed, resulting in

$$\mathbb{E}\{x_d[m_1]x_d^*[m_2]\} = 0, \ m_1 \neq m_2. \quad (47)$$

Based on these two assumptions, the expectation of $\chi(\tau, \nu)$ is given by

$$\mathbb{E}\{\chi(\tau, \nu)\} = \chi_{\mathrm{p}}(\tau, \nu) + \mathbb{E}\{\chi_{\mathrm{d}}(\tau, \nu)\}$$

$$= \begin{cases} P_{\mathrm{t}}, & \text{if } (\tau,\nu)=(0,0), \\ \chi_{\mathrm{p}}(\tau,\nu), & \text{otherwise,} \end{cases} \quad (48)$$

while the variance of $\chi(\tau,\nu)$ can be calculated as

$$\sigma^2_{\chi(\tau,\nu)} = \begin{cases} 2\sigma_d^2\sigma_p^2+(\mathbb{E}\{|x[0]|^4\}-\sigma_d^4)N_c, & \text{if}(\tau,\nu)=(0,0), \\ 2\sigma_d^2\sigma_p^2+\sigma_d^4 N_c, & \text{otherwise.} \end{cases}$$
$$(49)$$

The derivation of $\mathbb{E}\{\chi(\tau,\nu)\}$ is straightforward, and the derivation of $\sigma^2_{\chi(\tau,\nu)}$ is given in Appendix C.

Theorem 2: Given the number of subcarriers N_c, pilot power σ_{p}^2 and total data symbol power $P_{\mathrm{d}} = N_c\sigma_{\mathrm{d}}^2$, the ambiguity function variance $\sigma^2_{\chi(\tau,\nu)}$ of constant-modulus modulation schemes (e.g., QPSK) is always no larger than that of non-constant modulus modulation counterparts for arbitrary (τ,ν).

Proof: See Appendix D. $\square$

Theorem 3: Given the pilot power σ_{p}^2 and total data power P_{d}, when employing constant modulus modulation schemes, $\sigma^2_{\chi(\tau,\nu)}$ converges to zero as the number of subcarriers approaches infinity:

$$\lim_{N_c\to\infty}\sigma^2_{\chi(\tau,\nu)} = 0. \quad (50)$$

Proof: See Appendix E. $\square$

Remark 1: The inherent data randomness results in fluctuated mainlobe and sidelobes for the ambiguity function of AFDM-enabled ISAC signals, leading to possible missed detection or false alarms of targets. To reduce $\sigma^2_{\chi(\tau,\nu)}$ for sensing performance enhancement, we can employ constant modulus modulation schemes and increase the number of subcarriers according to Theorems 2 and 3.

IV. PILOT DESIGN FOR SENSING AND COMMUNICATION PERFORMANCE ENHANCEMENT

In addition to the variance, the expectation of the ambiguity function is also crucial for the target sensing performance. To minimize the false alarm probability, an ideal ambiguity function should have a prominent peak at $(0,0)$ and zero value at other grid points within Ω_{A}, i.e.,

$$\chi(\tau,\nu) = \begin{cases} P_{\mathrm{t}}, & \text{if } (\tau,\nu) = (0,0), \\ 0, & \text{if } (\tau,\nu) \in \Omega_A \neq (0,0). \end{cases} \quad (51)$$

As can be seen from (48), the expectation of the ambiguity function for the pilot-assisted AFDM signal is equal to the total power of the signal at $(0,0)$, while the values at other grid points are determined by the ambiguity function of the pilot signal. This phenomenon necessitates tailored design for the pilot sequence of the AFDM-enabled ISAC waveform. Before elaborating on the design, the following theorem validates that the AFDM pilots with an ideal ambiguity function can guarantee desirable communication performance level.

Theorem 4: When $2c_1 N_c$ is an integer, the pilot sequence with an ideal ambiguity function can achieve the optimal channel estimation performance by minimizing the mean squared error $\mathbb{E}\{\|\hat{\boldsymbol{\alpha}} - \boldsymbol{\alpha}\|^2\}$.

Proof: See Appendix F. $\square$

To ensure an ideal ambiguity function for the pilot sequence, existing studies insert sufficient zero guard samples between adjacent non-zero pilots in the DAFT domain. Specifically,

according to (42), to ensure the interference coefficient between two adjacent non-zero pilots is always zero within Ω_{A}, the neighboring pilot spacing Q should satisfy $Q > \max_{\tau,\nu} \mathrm{loc}^{(\tau,\nu)}$. Since $\Omega_{\mathrm{A}} = [-\tau_{\mathrm{m}}, \tau_{\mathrm{m}}] \times [-2\nu_{\mathrm{m}}, 2\nu_{\mathrm{m}}]$, the subcarrier offset $\mathrm{loc}^{(\tau,\nu)} \in [-2c_1\tau_{\mathrm{m}}N_c - 2\nu_{\mathrm{m}}, 2c_1\tau_{\mathrm{m}}N_c + 2\nu_{\mathrm{m}}]$, and the ambiguity function of the pilot sequence becomes ideal when the adjacent non-zero pilot spacing Q satisfies:

$$Q \geq 2c_1\tau_{\mathrm{m}}N_c + 2\nu_{\mathrm{m}} + 1. \quad (52)$$

For example, in [28], Q is set to $2c_1\tau_{\mathrm{m}}N_c + 2\nu_{\mathrm{m}} + 1$ and the number of non-zero pilots is chosen to be $N_{\mathrm{p}} = \lfloor \frac{N_c}{Q} \rfloor$. Inversely, when the pilot spacing Q is fixed, the maximum range of sensing and channel estimation is limited by

$$\tau_{\mathrm{m}} \leq \frac{Q - 2\nu_{\mathrm{m}} - 1}{2c_1 N_c}. \quad (53)$$

According to (53), small Q limits the capability boundary of both target sensing and channel estimation. On the other hand, the margin τ_{m} can be expanded by enlarging Q, which however sacrifices the number of non-zero pilots within a single AFDM symbol, causing degraded channel estimation accuracy. This dilemma makes the pilot assignment for AFDM rather challenging.

To overcome this challenge, we propose a novel pilot design in Theorem 5, which includes the choice of the parameter c_1 and the pilot spacing configuration as well as the pilot sequence design. The proposed pilot sequence features an ideal ambiguity function with the spacing Q independent of τ_{m}. As a result, our design enables simultaneous channel estimation and long-range target sensing both with superior accuracy.

Theorem 5: Consider an AFDM symbol with $N_c = 2^p$ subcarriers, where p is a non-zero integer. When $c_1 = \frac{2^q}{2N_c}$ with the integer q satisfying $2^{q-1} < 2\nu_{\mathrm{m}} + 1 \leq 2^q$, $Q = 2c_1\tilde{N}_c 2^r$ with $r = 0, 1, \cdots, p-q$, and $N_{\mathrm{p}} = N_c/Q$, the pilot signal satisfying the following equation has an ideal ambiguity function:

$$x_{\mathrm{p}}[m] = \begin{cases} \sqrt{\dfrac{\sigma_{\mathrm{p}}^2}{N_{\mathrm{p}}}} z\left[\dfrac{m}{Q}\right] e^{\mathrm{j}2\pi\psi[m]}, & m = 0, Q, \cdots, (N_{\mathrm{p}}-1)Q, \\ 0, & \text{otherwise,} \end{cases}$$
$$(54)$$

where $\psi[m] = \left(\frac{m^2 2^r}{2QN_c} - c_2 m^2\right)$, and $z[k]$ denotes any N_{p}-length CAZAC sequence [36], such as the Zadoff-Chu (ZC) sequence [37].

Proof: See Appendix G. $\square$

Remark 2: The advantage of the proposed pilot design lies in the fact that Q is independent of the maximum delay τ_{m}. As shown in Theorem 4, Q can be as small as $2c_1 N_c$, where c_1 depends solely on the maximum Doppler shift. Therefore, as τ_{m} increases, it is unnecessary to reduce the number of non-zero pilots, thus maintaining accurate channel estimation. In the following, we will give a specific example to illustrate how to obtain a pilot sequence based on Theorem 5. Firstly, an appropriate N_{p}-length CAZAC sequence should be chosen as the base sequence. Let us take the N_{p}-length ZC sequence as an example. According to Theorem 5, N_{p} is an even number, and thus the N_{p}-length ZC sequence can be written as

$$z[n] = e^{-\frac{\mathrm{j}\pi u n^2}{N}}, \quad n = 0, 1, \cdots, N_{\mathrm{p}}-1, \quad (55)$$

TABLE I

SIMULATIONS PARAMETERS

Symbol	Parameter	Value
f_c	Carrier frequency	28 GHz
N_c	Number of subcarriers	128
N_{cp}	Number of CPP	32
Δf	Subcarrier spacing	100 KHz
ν_m	Maximum normalized Doppler shift	2
τ_m	Maximum normalized delay	2 or 15
σ_p^2	Power of pilot	20 dB
σ_cn^2	Power of noise	30 dBm

where u is an integer satisfying $\gcd(N_\mathrm{p}, u) = 1$. Next, by substituting (55) in (54), the pilot signal can be expressed as

$$x_\mathrm{p}[m] = \begin{cases} \sqrt{\dfrac{\sigma_\mathrm{p}^2}{N_\mathrm{p}}} e^{-\frac{\mathrm{j}\pi u m^2}{N Q^2}} e^{\mathrm{j}2\pi \psi[m]}, & m = 0, Q, \cdots, (N_\mathrm{p}-1)Q, \\ 0, & \text{otherwise}, \end{cases}$$
(56)

Finally, we superpose the pilot signal on the data as (1) to obtain the transmit signal.

It should be noted that the proposed pilot design methodology is not equivalent to directly transforming the CAZAC sequence into the DAFT domain. CAZAC sequences ensure perfect auto-correlation property only when the Doppler shift is zero, and their autocorrelation performance deteriorates significantly under large Doppler shifts. Consequently, the sequence derived from directly transforming a CAZAC sequence cannot guarantee an ideal ambiguity function. In contrast, our proposed pilot is designed by exploiting the unique characteristics of AFDM. Due to its inherent multipath separation capability, interference between non-zero pilot symbols arises only from specific combinations of delay and Doppler shifts. We identify these critical delay-Doppler pairs and introduce appropriate phase shifts to the CAZAC sequences, enabling them to maintain ideal auto-correlation properties even under substantial Doppler shifts.

V. NUMERICAL RESULTS

Consider an AFDM system with $N_c = 128$ subcarriers, where each subcarrier carries a symbol modulated using QPSK. The key simulation parameters are summarized as Table I. We consider both the large-range scenario ($\tau_\mathrm{m} = 15$) and the small-range scenario ($\tau_\mathrm{m} = 2$). The maximum normalized Doppler frequency shift is set to $\nu_\mathrm{m} = 2$. The communication channel consists of $L = 3$ paths, with the normalized delay and Doppler shift of each path randomly selected from $[0, \tau_\mathrm{m}]$ and $[-\nu_\mathrm{m}, \nu_\mathrm{m}]$, respectively. The channel coefficient for each path follows a complex Gaussian distribution $\mathcal{CN} \sim (0, 1/L)$. For the sensing purpose, we consider a single-target model, where its normalized delay and Doppler shift are uniformly distributed within the ranges of $[0, \tau_\mathrm{m}]$ and $[-\nu_\mathrm{m}, \nu_\mathrm{m}]$, respectively. Numerical results are provided to validate the feasibility and superiority of the proposed pilot design in terms of both communication and sensing performance.
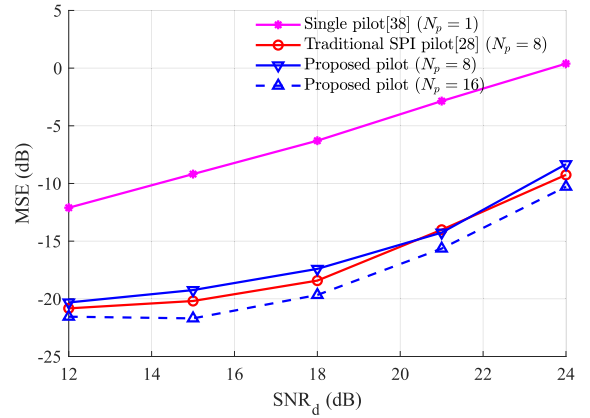

Fig. 5. Comparison of channel estimation performance between the proposed pilot design and existing designs under the scenario of $\tau_\mathrm{m} = 2$.

Fig. 6. Comparison of channel estimation performance between the proposed pilot design and existing designs under the scenario of $\tau_\mathrm{m} = 15$.
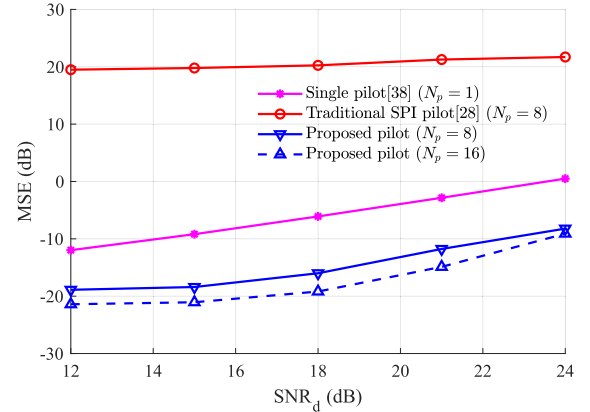
A. Communication Performance

Figs. 5 and 6 depict the channel estimation performances as the functions of the data signal-to-noise ratio $\mathrm{SNR}_\mathrm{d} = \sigma_\mathrm{d}^2/\sigma_\mathrm{cn}^2$ for the proposed pilot design and two existing designs under the scenarios of $\tau_\mathrm{m} = 2$ and $\tau_\mathrm{m} = 15$, respectively. The total power of pilot and noise signals are set as $\sigma_\mathrm{p}^2 = 20$ dB and $N_c \sigma_\mathrm{cn}^2 = 21$ dBm, respectively. The mean square error (MSE) is utilized to evaluate the channel estimation performance. It can be obtained by calculating the Frobenius norm of the difference between the channel matrix and its estimated value, which can be expressed as

$$\mathrm{MSE} = \sum_{i=0}^{N_\mathrm{iter}} \frac{||\mathbf{H}_\mathrm{c}^{(i)} - \hat{\mathbf{H}}_\mathrm{c}^{(i)}||}{N_\mathrm{iter}}.$$
(57)

Here $\mathbf{H}_\mathrm{c}^{(i)}$ and $\hat{\mathbf{H}}_\mathrm{c}^{(i)}$ denote the channel matrix and its estimated value for the i-th simulation run, and the results are averaged over $N_\mathrm{iter} = 10000$ simulation runs. In the single pilot design [38], there is only one non-zero pilot in the DAFT domain, which is put in the first subcarrier. The traditional SPI pilot denotes the superimposed pilot in [28] with $N_\mathrm{p} = 8$ non-zero pilots. For the proposed pilot design, as shown in (54), we consider $N_\mathrm{p} = 8$ and $N_\mathrm{p} = 16$. For a fair comparison, all the schemes adopt the same AFDM parameters with $c_1 = 4/N_c$ and $c_2 = \pi - 3$.

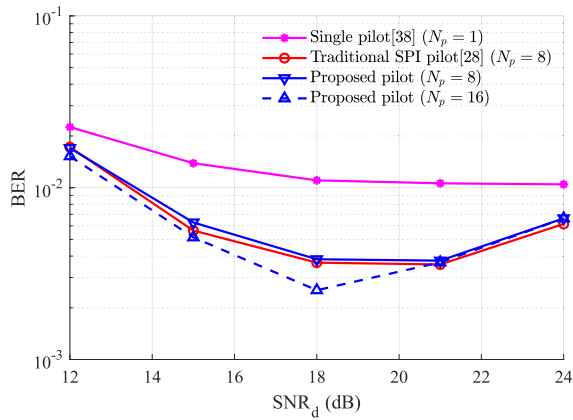It can be seen from Fig. 5 that as the data power increases, the equivalent noise power in channel estimation

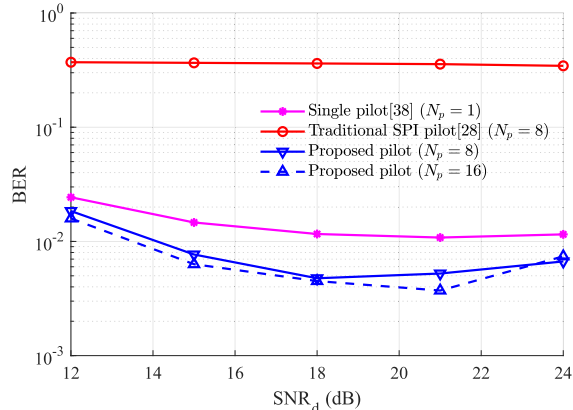Fig. 7. BER comparison between the proposed pilot design and existing designs under the scenario of $\tau_{\mathrm{m}} = 2$.

Fig. 8. BER comparison between the proposed pilot design and existing designs under $\tau_{\mathrm{m}} = 15$.
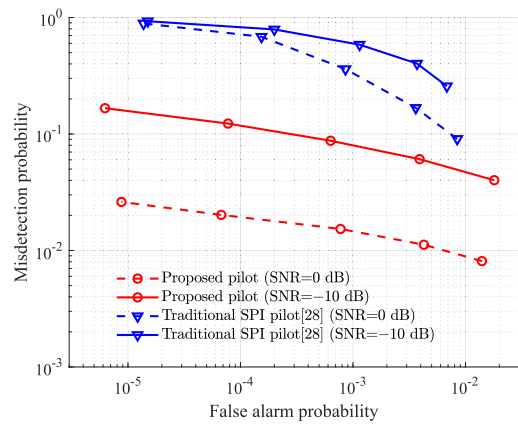

Fig. 9. ROC curve comparison between the proposed pilot and traditional SPI pilot designs under $\tau_{\mathrm{m}} = 15$ and given two different receive SNRs.

also increases, resulting in higher MSE for all the schemes. For the small-range scenario of $\tau_{\mathrm{m}} = 2$, both the proposed pilot design and the traditional SPI pilot with $N_{\mathrm{p}} = 8$ non-zero pilots achieve more accurate channel estimation results, with a 7 dB improvement in MSE compared to the single pilot scheme. This is because, when τ_{m} is relatively small, both the proposed pilot and traditional SPI pilot designs can realize the optimal channel estimation with no inter-pilot interference. Moreover, since the number of non-zero pilots in these designs is greater than that in the single pilot scheme, the UE can utilize more subcarriers for channel estimation, thereby achieving higher channel estimation accuracy. As expected, the proposed pilot design with $N_{\mathrm{p}} = 16$ outperforms the same design with $N_{\mathrm{p}} = 8$. On the other hand, for the large-range scenario of $\tau_{\mathrm{m}} = 15$, the traditional SPI pilot with $N_{\mathrm{p}} = 8$ no longer satisfies the requirements of (52). The received responses of two non-zero pilot symbols may overlap in the DAFT domain after passing through the channel, which leads to severe pilot interference and prevents the channel estimation from achieving the minimum mean square error performance. In contrast, the proposed pilot design maintains an ideal ambiguity function and ensures the optimal channel estimation with the similar MSEs in the both scenarios, as can be observed from Figs. 5 and 6.

Figs. 7 and 8 investigate the BER performance of the proposed pilot design and two existing designs under $\tau_{\mathrm{m}} = 2$ and $\tau_{\mathrm{m}} = 15$, respectively. Since the channel estimation performance of the single pilot design is considerably inferior

to those of the proposed pilot and traditional SPI pilot designs, its BER is much larger than those of the other two designs. As for our pilot and traditional SPI pilot designs, generally, for $\mathrm{SNR}_{\mathrm{d}} < 18$ dB, the BER reduces as $\mathrm{SNR}_{\mathrm{d}}$ increases but for $\mathrm{SNR}_{\mathrm{d}} > 21$ dB, the BER increases as $\mathrm{SNR}_{\mathrm{d}}$ increases. This is because for $\mathrm{SNR}_{\mathrm{d}} < 18$ dB, the channel estimation is relatively accurate, and increasing the data power improves the data demodulation performance. On the other hand, for $\mathrm{SNR}_{\mathrm{d}} > 21$ dB, as $\mathrm{SNR}_{\mathrm{d}}$ increases, the equivalent noise power for the channel estimation increases, leading to a decline in channel estimation accuracy and a corresponding rise in the BER. By comparing Figs. 7 and 8, it can be seen that as the maximum delay spread increases, the BER of the traditional SPI pilot increases significantly due to the degradation of its channel estimation performance. The proposed pilot design by contrast does not suffer from this performance degradation.

B. Sensing Performance

The ROC curves of the proposed pilot and traditional SPI pilot designs are illustrated in Fig. 9 under the large-range scenario of $\tau_{\mathrm{m}} = 15$, where the receive SNR at the ISAC receiver is set to 0 dB or -10 dB. Both the proposed pilot and traditional SPI pilot designs have $N_{\mathrm{p}} = 8$ non-zero pilots. To obtain the ROC curve, we vary the threshold γ in (24) and record the corresponding probabilities of false alarm and missed detection, as shown in Fig. 9. We define a missed detection event as either failing to detect the peak corresponding to the target or when the difference between the estimated normalized delay (or normalized Doppler shift) and the true value exceeds 1. Since the traditional SPI pilot cannot ensure an ideal ambiguity function under $\tau_{\mathrm{m}} = 15$, its ROC curve is much inferior to that of the proposed pilot design, i.e., the probability of missed detection of the traditional SPI pilot is much higher than that of the proposed pilot at the same false alarm probability. Due to its ideal ambiguity function, the performance of the proposed pilot design is not limited by high sidelobes but is primarily determined by the receive SNR. As a result, when the SNR increases, the proposed scheme exhibits a significant improvement in sensing performance.

Figs. 10(a) and 10(b) compare the simulated distance root MSE (RMES$_R$) and velocity root MSE (RMES$_V$) with $\sqrt{\mathrm{CRB}_R}$ and $\sqrt{\mathrm{CRB}_V}$, respectively, where the carrier frequency is set to $f_c = 28$ GHz and the sensing range is set to

(a) Comparison between RMES_R and $\sqrt{\text{CRB}_R}$.

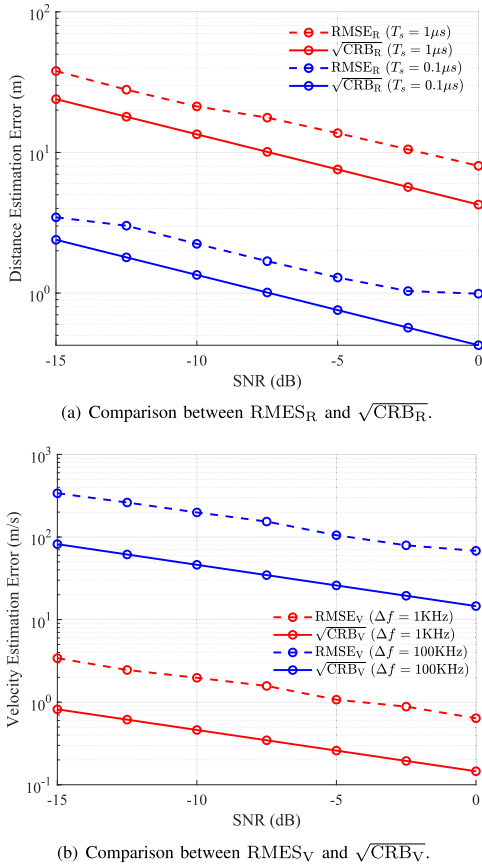(b) Comparison between RMES_V and $\sqrt{\text{CRB}_V}$.

Fig. 10. Comparison of the simulated RMSE and the square root of CRB.

$\tau_m = 15$. Specifically, $\sqrt{\text{CRB}_R}$ and $\sqrt{\text{CRB}_V}$ are calculated by averaging CRB_R and CRB_V for any possible $\bar\tau$, respectively, and deriving the square root of the results. It can be seen from Fig. 10(a) that as the sampling period decreases, the distance estimation error reduces, which agrees with (36). From Fig. 10(b), it can be seen that as the subcarrier spacing decreases, the velocity estimation error reduces, which agrees with (37). Moreover, it can be observed that both RMES_R and RMES_V are close to the square roots of derived CRBs, demonstrating that the proposed pilot design enables high-precision sensing.

VI. Conclusion

In this paper, we have presented a theoretical framework for AFDM-enabled ISAC systems and introduced a novel pilot design for pilot-assisted AFDM waveforms to enhance both communication and sensing performance. Specifically, we derived closed-form CRB expressions for target sensing in AFDM, offering helpful guidelines for system design and insights into the advantages of AFDM over existing alternatives. Furthermore, we have formulated the ambiguity function of the pilot-assisted AFDM waveform for the first time and analyzed its statistical properties. To overcome the sensing range limitations imposed by pilot spacing, we have also proposed a novel superimposed pilot design, which has been analytically proven to achieve an ideal ambiguity function and optimal channel estimation simultaneously. Numerical results have been provided to validate the theoretical derivations and demonstrate the superiority of the proposed pilot design.

Appendix

A. Derivation of FIM

First we provide a detailed derivation of $\frac{\partial \bar s[n]}{\partial \bar\tau}$:

$$\frac{\partial \bar s[n]}{\partial \bar\tau} = \beta \frac{\partial \bar s(nT_s - \bar\tau T_s)}{\partial \bar\tau} e^{j2\pi\bar\nu n/N_c}$$

$$= \frac{\beta e^{j2\pi\bar\nu n/N_c}}{\sqrt{N_c}} \sum_{m=0}^{N_c-1} \left(j2\pi \frac{\partial g_m(nT_s - \bar\tau T_s)}{\partial \bar\tau} \right) x[m]$$

$$\times e^{j2\pi\left(g_m(nT_s - \bar\tau T_s) + c_2 m^2 \right)}. \quad (58)$$

We note

$$\frac{\partial g_m(nT_s - \bar\tau T_s)}{\partial \bar\tau} = -T_s \frac{\partial g_m(t)}{\partial t}\Big|_{t=nT_s - \bar\tau T_s}, \quad (59)$$

with

$$\frac{\partial g_m(t)}{\partial t} = \frac{2c_1 t}{T_s^2} + \frac{m}{N_c T_s} - q_m\left(\frac{t}{T_s}\right)\frac{1}{T_s} - \frac{\partial q_m\left(\frac{t}{T_s}\right)}{\partial t}\frac{t}{T_s}. \quad (60)$$

Since $q_m\left(\frac{t}{T_s}\right) = \left\lfloor 2c_1\frac{t}{T_s} + \frac{m}{N_c} \right\rfloor$, $\frac{\partial q_m\left(\frac{t}{T_s}\right)}{\partial t}$ takes the value of 0 in most cases, and it can be dropped from (60) for approximation. Therefore, we have

$$\frac{\partial g_m(nT_s - \bar\tau T_s)}{\partial \bar\tau} \approx -2\, c_1(n-\bar\tau) - \frac{m}{N_c} + \left\lfloor 2\, c_1(n-\bar\tau) + \frac{m}{N_c} \right\rfloor$$

$$\triangleq -\mathcal{F}_m(n - \bar\tau). \quad (61)$$

Substituting (61) into (58) yields (32).

Based on the above calculation results, we can compute $\mathbf{F_I}$. Take $F_I[1,1]$ as an example, which can be derived as

$$F_I[1,1] = \frac{2}{\sigma_s^2} \Re\left\{ \mathbb{E}\left\{ \sum_{n=0}^{N_c-1} \left| s(nT_s - \bar\tau T_s) e^{j2\pi\bar\nu n/N_c} \right|^2 \right\} \right\}$$

$$= \frac{2}{\sigma_s^2 N_c^2} \Re\left\{ \sum_{m_1=0}^{N_c-1}\sum_{m_2=0}^{N_c-1} \mathbb{E}\left\{ x[m_1]x^*[m_2] \right\} \right.$$

$$\left. \times \left(\sum_{n=-\bar\tau}^{N_c-1-\bar\tau} e^{j2\pi(\eta_{m_1}[n] - \eta_{m_2}[n])} \right) \right\}. \quad (62)$$

Since $\sum_{n=-\bar\tau}^{N_c-1-\bar\tau} e^{j2\pi(\eta_{m_1}[n] - \eta_{m_2}[n])} = 0$ for $m_1 \neq m_2$, (62) can be further simplified as

$$F_I[1,1] = \frac{2}{\sigma_s^2 N_c^2} \Re\left\{ N_c \sum_{m_1=0}^{N_c-1} \mathbb{E}\{|x[m_1]|^2\} \right\} = \frac{2P_t}{\sigma_s^2 N_c}, \quad (63)$$

where $P_m = \mathbb{E}\{|x[m]|^2\}$ and $P_t = \sum_{m=0}^{N_c-1} P_m$. Other elements of $\mathbf{F_I}$ can be calculated using similar approaches, which are omitted for brevity. By combining all the elements, we obtain the FIM (33).

B. Proof of Theorem 1

Proof: By substituting $x[m] = x_p[m] + x_d[m]$ into (40), we have

$$\chi(\tau, \nu)$$

$$= C_2 \bigg(\sum_{m_1=0}^{N_c-1}\sum_{m_2=0}^{N_c-1} x_p^*[m_1]x_p[m_2] e^{-\frac{j2\pi m_2\tau}{N_c}} S^{(\tau,\nu)}(m_1, m_2)$$

$$+ \sum_{m_1=0}^{N_c-1}\sum_{m_2=0}^{N_c-1} x_{\mathrm{d}}^*[m_1]x_{\mathrm{d}}[m_2]e^{-\frac{\mathrm{j}2\pi m_2\tau}{N_c}}S^{(\tau,\nu)}(m_1,m_2)$$

$$+ \sum_{m_1=0}^{N_c-1}\sum_{m_2=0}^{N_c-1} x_{\mathrm{d}}^*[m_1]x_{\mathrm{p}}[m_2]e^{-\frac{\mathrm{j}2\pi m_2\tau}{N_c}}S^{(\tau,\nu)}(m_1,m_2)$$

$$+ \sum_{m_1=0}^{N_c-1}\sum_{m_2=0}^{N_c-1} x_{\mathrm{p}}^*[m_1]x_{\mathrm{d}}[m_2]e^{-\frac{\mathrm{j}2\pi m_2\tau}{N_c}}S^{(\tau,\nu)}(m_1,m_2)\Bigg). \quad (64)$$

According to the definition of ambiguity function, the first and second terms of (64) are the ambiguity functions of the pilot ($\chi_{\mathrm{p}}(\tau,\nu)$) and data signal ($\chi_{\mathrm{d}}(\tau,\nu)$), respectively. This completes the proof. $\qquad\square$

C. Derivation of $\sigma^2_{\chi(\tau,\nu)}$

The variance of $\chi(\tau,\nu)$ is given by

$$\sigma^2_{\chi(\tau,\nu)} = \mathbb{E}\{|\chi(\tau,\nu)|^2\} - |\mathbb{E}\{\chi(\tau,\nu)\}|^2. \quad (65)$$

Given the assumptions $\mathbb{E}\{x_{\mathrm{d}}[m]\} = 0$ and $\mathbb{E}\{x_{\mathrm{d}}^2[m_1]\} = 0$, any term of $\mathbb{E}\{|\chi(\tau,\nu)|^2\}$ containing $\mathbb{E}\{x_{\mathrm{d}}[m]\}$ and $\mathbb{E}\{x_{\mathrm{d}}^2[m_1]\}$ is zero. Therefore,

$$\mathbb{E}\{|\chi(\tau,\nu)|^2\} = |\chi_{\mathrm{p}}(\tau,\nu)|^2 + \mathbb{E}\{|\chi_{\mathrm{d}}(\tau,\nu)|^2\}$$
$$+ \mathbb{E}\{|\chi_{\mathrm{dp}}(\tau,\nu)|^2\} + \mathbb{E}\{|\chi_{\mathrm{pd}}(\tau,\nu)|^2\}$$
$$+ \mathbb{E}\{2\Re\{\chi_{\mathrm{p}}(\tau,\nu)\chi_{\mathrm{d}}^*(\tau,\nu)\}\}. \quad (66)$$

According to (48),

$$|\mathbb{E}\{\chi(\tau,\nu)\}|^2 = |\chi_{\mathrm{p}}(\tau,\nu)|^2 + |\mathbb{E}\{\chi_{\mathrm{d}}(\tau,\nu)\}|^2$$
$$+ \mathbb{E}\{2\Re\{\chi_{\mathrm{p}}(\tau,\nu)\chi_{\mathrm{d}}^*(\tau,\nu)\}\}. \quad (67)$$

By substituting (66) and (67) into (65), we obtain

$$\sigma^2_{\chi(\tau,\nu)} = \sigma^2_{\chi_{\mathrm{d}}(\tau,\nu)} + \mathbb{E}\{|\chi_{\mathrm{dp}}(\tau,\nu)|^2\} + \mathbb{E}\{|\chi_{\mathrm{pd}}(\tau,\nu)|^2\}. \quad (68)$$

The first term in (68) can be derived as

$$\sigma^2_{\chi_{\mathrm{d}}(\tau,\nu)} = \frac{1}{N_c^2}\Bigg(\sum_{m_1=0}^{N_c-1}\sum_{m_2\neq m_1}^{N_c-1} \sigma_d^4|S^{(\tau,\nu)}(m_1,m_2)|^2$$
$$+ \sum_{m=0}^{N_c-1}\big(\mathbb{E}\{|x[m]|^4\}-\sigma_d^4\big)|S^{(\tau,\nu)}(m,m)|^2\Bigg). \quad (69)$$

The second term in (68) is equal to the third term, which can be expressed as

$$\mathbb{E}\{|\chi_{\mathrm{dp}}(\tau,\nu)|^2\}$$
$$= \frac{1}{N_c^2}\sum_{m_1=0}^{N_c-1}\sum_{m_2=0}^{N_c-1}\sigma_d^2|x_{\mathrm{p}}[m_2]|^2|S^{(\tau,\nu)}(m_1,m_2)|^2. \quad (70)$$

According to (42), $|S^{(\tau,\nu)}(m_1,m_2)|^2$ can be calculated as

$$|S^{(\tau,\nu)}(m_1,m_2)|^2 = \begin{cases} N_c^2, & \text{if } \langle m_2-m_1\rangle_{N_c} = \mathrm{loc}^{(\tau,\nu)}, \\ 0, & \text{otherwise.} \end{cases} \quad (71)$$

Therefore, when $(\tau,\nu)=(0,0)$, we obtain

$$\sigma^2_{\chi(\tau,\nu)} = N_c\big(\mathbb{E}\{|x[m]|^4\}-\sigma_d^4\big) + 2\sigma_d^2\sum_{m_1=0}^{N_c-1}|x_{\mathrm{p}}[m_1]|^2$$
$$= N_c\big(\mathbb{E}\{|x[0]|^4\}-\sigma_d^4\big) + 2\sigma_d^2\sigma_{\mathrm{p}}^2. \quad (72)$$

When $(\tau,\nu)\neq(0,0)$, we have

$$\sigma^2_{\chi(\tau,\nu)} = \sum_{m_1=0}^{N_c-1}\sigma_d^4 + 2\sigma_d^2\sum_{m_1=0}^{N_c-1}\big|x_{\mathrm{p}}[\langle m_1+\mathrm{loc}^{(\tau,\nu)}\rangle_{N_c}]\big|^2$$
$$= N_c\sigma_d^4 + 2\sigma_d^2\sigma_{\mathrm{p}}^2. \quad (73)$$

D. Proof of Theorem 2

Proof: As seen in (49), when $(\tau,\nu)\neq(0,0)$, the variance is irrelevant to specific modulation method. On the other hand, when $(\tau,\nu)=(0,0)$, the variance can be reduced by minimizing the fourth moment of the constellation's amplitude, i.e., $\mathbb{E}\{|x[0]|^4\}$. According to the Cauchy-Schwarz inequality, the fourth moment is no less than the square of the second moment, i.e., $\mathbb{E}\{|x[0]|^4\}\geq\sigma_{\mathrm{d}}^4$. Furthermore, $\mathbb{E}\{|x[0]|^4\}=\sigma_{\mathrm{d}}^4$ if and only if the constellation points have constant modulus. Therefore, by employing the constant-modulus modulation, the ambiguity function variance is minimized for $(\tau,\nu)=(0,0)$. This completes the proof. $\qquad\square$

E. Proof of Theorem 3

Proof: By choosing $\sigma_{\mathrm{d}}^2 = P_{\mathrm{d}}/N_c$ and $\mathbb{E}\{|x[0]|^4\}=\sigma_d^4$ in (49), the variance can be written as

$$\sigma^2_{\chi(\tau,\nu)} = \begin{cases} 2\dfrac{P_{\mathrm{d}}\sigma_p^2}{N_c}, & \text{if}(\tau,\nu)=(0,0), \\[2mm] 2\dfrac{P_{\mathrm{d}}\sigma_p^2}{N_c}+\dfrac{P_{\mathrm{d}}^2}{N_c}, & \text{otherwise.} \end{cases} \quad (74)$$

For $(\tau,\nu)=(0,0)$,

$$\lim_{N_c\to\infty}\sigma^2_{\chi(\tau,\nu)} = \lim_{N_c\to\infty}2\frac{P_{\mathrm{d}}\sigma_p^2}{N_c} = 0. \quad (75)$$

For $(\tau,\nu)\neq(0,0)$

$$\lim_{N_c\to\infty}\sigma^2_{\chi(\tau,\nu)} = \lim_{N_c\to\infty}2\frac{P_{\mathrm{d}}\sigma_p^2}{N_c}+\frac{P_{\mathrm{d}}^2}{N_c} = 0. \quad (76)$$

This completes the proof. $\qquad\square$

F. Proof of Theorem 4

Proof: In [28], it has been proved that the minimal $\mathbb{E}\{\|\hat{\boldsymbol{\alpha}}-\boldsymbol{\alpha}\|^2\}$ can be achieved when the column vectors of the matrix $\boldsymbol{\Psi}_{\mathrm{p}}$ in (17) are orthogonal with each other. We now prove that a pilot sequence $\mathbf{x}_{\mathrm{p}}$ with an ideal ambiguity function always ensures that any two column vectors of $\boldsymbol{\Psi}_{\mathrm{p}}$ are mutually orthogonal. The inner product between the i-th and j-th columns of $\boldsymbol{\Psi}_{\mathrm{p}}$ for $i\neq j$ can be expressed as

$$\mathbf{x}_{\mathrm{p}}^{\mathrm{H}}\boldsymbol{\Phi}_i^{\mathrm{H}}\boldsymbol{\Phi}_j\mathbf{x}_{\mathrm{p}}$$
$$= \mathbf{x}_{\mathrm{p}}\mathbf{A}\big(\boldsymbol{\Gamma}_{\mathrm{CPP}_i}\boldsymbol{\Pi}^{\tau_i}\boldsymbol{\Delta}_{\nu_i}\big)^{\mathrm{H}}\boldsymbol{\Gamma}_{\mathrm{CPP}_j}\boldsymbol{\Pi}^{\tau_j}\boldsymbol{\Delta}_{\nu_j}\mathbf{A}^{\mathrm{H}}\mathbf{x}_{\mathrm{p}}$$
$$= \mathbf{x}_{\mathrm{p}}\mathbf{A}\boldsymbol{\Delta}_{-\nu_i}\boldsymbol{\Pi}^{N_c-\tau_i}\boldsymbol{\Gamma}_{\mathrm{CPP}_i}^{\mathrm{H}}\boldsymbol{\Gamma}_{\mathrm{CPP}_j}\boldsymbol{\Pi}^{\tau_j}\boldsymbol{\Delta}_{\nu_j}\mathbf{A}^{\mathrm{H}}\mathbf{x}_{\mathrm{p}}. \quad (77)$$

When $2c_1N_c$ is an integer, $\boldsymbol{\Gamma}_{\mathrm{CPP}_i} = \mathbf{I}_{N_c}$. According to the definitions of $\boldsymbol{\Pi}^{\tau_i}$ and $\boldsymbol{\Delta}_{\nu_i}$, $\boldsymbol{\Pi}^{\tau_i}\boldsymbol{\Delta}_{\nu_i} = e^{-\mathrm{j}2\pi\nu_i\tau_i/N}\boldsymbol{\Delta}_{\nu_i}\boldsymbol{\Pi}^{\tau_i}$. Based on these properties, $\mathbf{x}_{\mathrm{p}}^{\mathrm{H}}\boldsymbol{\Phi}_i^{\mathrm{H}}\boldsymbol{\Phi}_j\mathbf{x}_{\mathrm{p}}$ can be simplified as

$$\mathbf{x}_{\mathrm{p}}^{\mathrm{H}}\boldsymbol{\Phi}_i^{\mathrm{H}}\boldsymbol{\Phi}_j\mathbf{x}_{\mathrm{p}} = \mathbf{x}_{\mathrm{p}}\mathbf{A}\boldsymbol{\Delta}_{-\nu_i}\boldsymbol{\Pi}^{\tau_j-\tau_i}\boldsymbol{\Delta}_{\nu_j}\mathbf{A}^{\mathrm{H}}\mathbf{x}_{\mathrm{p}}$$
$$= e^{-\mathrm{j}2\pi\nu_i(\tau_j-\tau_i)/N}\mathbf{x}_{\mathrm{p}}\mathbf{A}\boldsymbol{\Delta}_{\nu_j-\nu_i}\boldsymbol{\Pi}^{\tau_j-\tau_i}\mathbf{A}^{\mathrm{H}}\mathbf{x}_{\mathrm{p}}. \quad (78)$$

(78) can be interpreted as the cross-correlation between the pilot sequence with its corresponding echo obtained with a time delay of $\hat{\tau} = \tau_j - \tau_i$ and Doppler shift of $\hat{\nu} = \tau_j - \tau_i$, which is aligned with the ambiguity function definition. Therefore, (78) can be equivalently rewritten as

$$\mathbf{x}_{\mathrm{p}}^{\mathrm{H}}\boldsymbol{\Phi}_i^{\mathrm{H}}\boldsymbol{\Phi}_j\mathbf{x}_{\mathrm{p}} = e^{-\mathrm{j}2\pi\nu_i\hat{\tau}/N}\chi_{\mathrm{p}}(\hat{\tau},\hat{\nu}). \quad (79)$$

Since $(\tau_i,\nu_i),(\tau_j,\nu_j)\in\Omega_{\mathrm{R}}$, we have $(\hat{\tau},\hat{\nu})\in\Omega_{\mathrm{A}}$. Furthermore, $(\hat{\tau},\hat{\nu})\neq(0,0)$ for $i\neq j$. According to the definition of ideal ambiguity function, $\mathbf{x}_{\mathrm{p}}^{\mathrm{H}}\boldsymbol{\Phi}_i^{\mathrm{H}}\boldsymbol{\Phi}_j\mathbf{x}_{\mathrm{p}}=0$. □

G. Proof of Theorem 5

Proof: The ambiguity function of the proposed pilot sequence can be expressed as

$$\chi_{\mathrm{p}}(\tau,\nu) = C_2\sum_{k_1=0}^{N_{\mathrm{P}}}\sum_{k_2=0}^{N_{\mathrm{P}}}x_p^*[k_1Q]x_p[k_2Q]e^{-\mathrm{j}2\pi\frac{k_2Q\tau}{N_c}}$$
$$\times S(k_1Q,k_2Q,\tau,\nu). \quad (80)$$

According to (42), $S(k_1Q,k_2Q,\tau,\nu)$ is non-zero if and only if $\langle k_2Q - k_1Q\rangle_{N_c}=\mathrm{loc}^{(\tau,\nu)}$. Based on this property, we discuss the value of $\chi_{\mathrm{p}}(\tau,\nu)$ in the following two cases.

Case 1: When Q cannot divide $\mathrm{loc}^{(\tau,\nu)}$, there do not exist values of k_1 and k_2 that satisfy equation $\langle k_2Q - k_1Q\rangle_{N_c}=\mathrm{loc}^{(\tau,\nu)}$, since $\langle k_2Q - k_1Q\rangle_{N_c}$ is always a multiple of Q. Therefore, $S(k_1Q,k_2Q,\tau,\nu)$ is always zero and $\chi_{\mathrm{p}}(\tau,\nu)=0$.

Case 2: When Q can divide $\mathrm{loc}^{(\tau,\nu)}$, there exists an integer $\hat{k}$ satisfying $\mathrm{loc}^{(\tau,\nu)}=\hat{k}Q$. By recalling the expressions of $\mathrm{loc}^{(\tau,\nu)}$ and Q, we obtain

$$2\,c_1N_c2^r\hat{k} = 2\,c_1\tau N_c - \nu. \quad (81)$$

Based on the multipath separation ability of AFDM in the DAFT domain, i.e., if $\tau_1\neq\tau_2$ or $\nu_1\neq\nu_2$, $\mathrm{loc}^{(\tau_1,\nu_1)}\neq\mathrm{loc}^{(\tau_2,\nu_2)}$, the only solution of (81) is $(\tau,\nu)=(2^r\hat{k},0)$. By substituting this solution into the (80), the expression is simplified as

$$\chi_{\mathrm{p}}(\tau,\nu)=\chi_{\mathrm{p}}(2^r\hat{k},0)=C_3\sum_{k_1=0}^{N_{\mathrm{P}}}x_p^*[k_1Q]x_p[\langle k_1Q+\hat{k}Q\rangle_{N_c}]$$
$$\times e^{-\mathrm{j}2\pi\frac{(k_1Q+\hat{k}Q)2^r\hat{k}}{N_c}}e^{\mathrm{j}2\pi c_2Q^2(2k_1\hat{k})}, \quad (82)$$

where $C_3=C_2N_ce^{\mathrm{j}2\pi c_2Q^2\hat{k}^2}$. Using $x_{\mathrm{p}}[m]$ of (54) in (82) leads to

$$\chi_{\mathrm{p}}(2^r\hat{k},0) = C_4\sum_{k_1=0}^{N_{\mathrm{P}}}z^*[k_1]z[\langle k_1+\hat{k}\rangle_{N_{\mathrm{P}}}], \quad (83)$$

where $C_4=C_2N_c\frac{\sigma_{\mathrm{p}}^2}{N_{\mathrm{P}}}e^{-\mathrm{j}2\pi\frac{\hat{k}^22^rQ}{2N_c}}$. Since $z[k]$ is a CAZAC sequence, we have $\chi_{\mathrm{p}}(2^r\hat{k},0)=0$ when $\hat{k}\neq0$, which means $\chi_{\mathrm{p}}(\tau,\nu)=0$ when $(\tau,\nu)\neq(0,0)$. By combining the conclusions of Case 1 and Case 2, the value of $\chi_{\mathrm{p}}(\tau,\nu)$ is non-zero only at $(\tau,\nu)=(0,0)$. Therefore, the proposed pilot design, which satisfies (54), can ensure an ideal ambiguity function. □

REFERENCES

[1] F. Liu et al., "Integrated sensing and communications: Toward dual-functional wireless networks for 6G and beyond," *IEEE J. Sel. Areas Commun.*, vol. 40, no. 6, pp. 1728–1767, Jun. 2022.

[2] Y. Cui, F. Liu, X. Jing, and J. Mu, "Integrating sensing and communications for ubiquitous IoT: Applications, trends, and challenges," *IEEE Netw.*, vol. 35, no. 5, pp. 158–167, Sep. 2021.

[3] F. Dong, F. Liu, Y. Cui, W. Wang, K. Han, and Z. Wang, "Sensing as a service in 6G perceptive networks: A unified framework for ISAC resource allocation," *IEEE Trans. Wireless Commun.*, vol. 22, no. 5, pp. 3522–3536, May 2023.

[4] N. González-Prelcic et al., "The integrated sensing and communication revolution for 6G: Vision, techniques, and applications," *Proc. IEEE*, vol. 112, no. 7, pp. 676–723, Jul. 2024.

[5] J. Zhao, S. Xue, K. Cai, X. Mu, Y. Liu, and Y. Zhu, "Near-field integrated sensing and communications for secure UAV networks," 2025, *arXiv:2502.01003*.

[6] W. Zhou, R. Zhang, G. Chen, and W. Wu, "Integrated sensing and communication waveform design: A survey," *IEEE Open J. Commun. Soc.*, vol. 3, pp. 1930–1949, 2022.

[7] F. Liu et al., "Seventy years of radar and communications: The road from separation to integration," *IEEE Signal Process. Mag.*, vol. 40, no. 5, pp. 106–121, Jul. 2023.

[8] S. Li, F. Zhang, T. Mao, R. Na, Z. Wang, and G. K. Karagiannidis, "Transmit beamforming design for ISAC with stacked intelligent metasurfaces," *IEEE Trans. Veh. Technol.*, vol. 74, no. 4, pp. 6767–6772, Apr. 2025, doi: 10.1109/TVT.2024.3517709.

[9] F. Zhang et al., "Multicarrier waveform design for mmWave/THz integrated sensing and communication," in *Proc. Int. Wireless Commun. Mobile Comput. (IWCMC)*, Cyprus, May 2024, pp. 501–506.

[10] A. Kaushik et al., "Toward integrated sensing and communications for 6G: Key enabling technologies, standardization, and challenges," *IEEE Commun. Standards Mag.*, vol. 8, no. 2, pp. 52–59, Jun. 2024.

[11] X. Zhang, Z. Lu, and J. Wang, "Sensing-aided CSI feedback with deep learning for massive MIMO systems," in *Proc. IEEE Int. Conf. Commun.*, Denver, CO, USA, Jun. 2024, pp. 2282–2287.

[12] T. Mao, J. Chen, Q. Wang, C. Han, Z. Wang, and G. K. Karagiannidis, "Waveform design for joint sensing and communications in millimeter-wave and low terahertz bands," *IEEE Trans. Commun.*, vol. 70, no. 10, pp. 7023–7039, Oct. 2022.

[13] V. Koivunen, M. F. Keskin, H. Wymeersch, M. Valkama, and N. González-Prelcic, "Multicarrier ISAC: Advances in waveform design, signal processing, and learning under nonidealities," *IEEE Signal Process. Mag.*, vol. 41, no. 5, pp. 17–30, Sep. 2024.

[14] F. Zhang, T. Mao, R. Liu, Z. Han, S. Chen, and Z. Wang, "Cross-domain dual-functional OFDM waveform design for accurate sensing/positioning," *IEEE J. Sel. Areas Commun.*, vol. 42, no. 9, pp. 2259–2274, Sep. 2024.

[15] C. Shi, Y. Wang, F. Wang, S. Salous, and J. Zhou, "Joint optimization scheme for subcarrier selection and power allocation in multicarrier dual-function radar-communication system," *IEEE Syst. J.*, vol. 15, no. 1, pp. 947–958, Mar. 2021.

[16] Y. Chen, G. Liao, Y. Liu, H. Li, and X. Liu, "Joint subcarrier and power allocation for integrated OFDM waveform in RadCom systems," *IEEE Commun. Lett.*, vol. 27, no. 1, pp. 253–257, Jan. 2023.

[17] F. Zhang et al., "Cross-domain multicarrier waveform design for integrated sensing and communication," in *Proc. IEEE Wireless Commun. Netw. Conf. (WCNC)*, Dubai, United Arab Emirates, Apr. 2024, pp. 1–6.

[18] H. Yin, X. Wei, Y. Tang, and K. Yang, "Diagonally reconstructed channel estimation for MIMO-AFDM with inter-Doppler interference in doubly selective channels," *IEEE Trans. Wireless Commun.*, vol. 23, no. 10, pp. 14066–14079, Oct. 2024.

[19] L. Gaudio, M. Kobayashi, G. Caire, and G. Colavolpe, "On the effectiveness of OTFS for joint radar parameter estimation and communication," *IEEE Trans. Wireless Commun.*, vol. 19, no. 9, pp. 5951–5965, Sep. 2020.

[20] M. F. Keskin, C. Marcus, O. Eriksson, A. Alvarado, J. Widmer, and H. Wymeersch, "Integrated sensing and communications with MIMO-OTFS: ISI/ICI exploitation and delay-Doppler multiplexing," *IEEE Trans. Wireless Commun.*, vol. 23, no. 8, pp. 10229–10246, Aug. 2024.

[21] X. Ouyang and J. Zhao, "Orthogonal chirp division multiplexing," *IEEE Trans. Commun.*, vol. 64, no. 9, pp. 3946–3957, Sep. 2016.

[22] L. G. D. Oliveira, M. B. Alabd, B. Nuss, and T. Zwick, "An OCDM radar-communication system," in *Proc. 14th Eur. Conf. Antennas Propag. (EuCAP)*, Copenhagen, Denmark, Mar. 2020, pp. 1–5.

[23] A. Bemani, N. Ksairi, and M. Kountouris, "Affine frequency division multiplexing for next generation wireless communications," *IEEE Trans. Wireless Commun.*, vol. 22, no. 11, pp. 8214–8229, Nov. 2023.

[24] H. Bao, H. Zhuang, Z. Wang, and G. Pang, "Performance trade-off between communication and sensing based on AFDM parameter adjustment," in *Proc. IEEE 35th Int. Symp. Pers., Indoor Mobile Radio Commun. (PIMRC)*, Valencia, Spain, Sep. 2024, pp. 1–6.

[25] J. Zhu, Y. Tang, F. Liu, X. Zhang, H. Yin, and Y. Zhou, "AFDM-based bistatic integrated sensing and communication in static scatterer environments," *IEEE Wireless Commun. Lett.*, vol. 13, no. 8, pp. 2245–2249, Aug. 2024.

[26] Y. Ni, Z. Wang, P. Yuan, and Q. Huang, "An AFDM-based integrated sensing and communications," in *Proc. Int. Symp. Wireless Commun. Syst. (ISWCS)*, Hangzhou, China, Oct. 2022, pp. 1–6.

[27] A. Bemani, N. Ksairi, and M. Kountouris, "Integrated sensing and communications with affine frequency division multiplexing," *IEEE Wireless Commun. Lett.*, vol. 13, no. 5, pp. 1255–1259, May 2024.

[28] K. Zheng, M. Wen, T. Mao, L. Xiao, and Z. Wang, "Channel estimation for AFDM with superimposed pilots," *IEEE Trans. Veh. Technol.*, vol. 74, no. 2, pp. 3389–3394, Feb. 2025, doi: 10.1109/TVT.2024.3469380.

[29] C. Baquero Barneto et al., "Full-duplex OFDM radar with LTE and 5G NR waveforms: Challenges, solutions, and measurements," *IEEE Trans. Microw. Theory Techn.*, vol. 67, no. 10, pp. 4042–4054, Oct. 2019.

[30] H. Yin et al., "Affine frequency division multiplexing: Extending OFDM for scenario-flexibility and resilience," 2025, *arXiv:2502.04735*.

[31] F. Zhang, T. Mao, and Z. Wang, "Doppler-resilient design of CAZAC sequences for mmWave/THz sensing applications," *IEEE Trans. Veh. Technol.*, vol. 73, no. 2, pp. 2878–2883, Feb. 2024.

[32] C. Sturm, T. Zwick, and W. Wiesbeck, "An OFDM system concept for joint radar and communications operations," in *Proc. IEEE 69th Veh. Technol. Conf.*, Barcelona, Spain, Apr. 2009, pp. 1–5.

[33] T. Ma, Y. Xiao, X. Lei, and M. Xiao, "Integrated sensing and communication for wireless extended reality (XR) with reconfigurable intelligent surface," *IEEE J. Sel. Topics Signal Process.*, vol. 17, no. 5, pp. 980–994, Sep. 2023.

[34] M. Kronauge and H. Rohling, "Fast two-dimensional CFAR procedure," *IEEE Trans. Aerosp. Electron. Syst.*, vol. 49, no. 3, pp. 1817–1823, Jul. 2013.

[35] Z. Ye, Z. Zhou, P. Fan, Z. Liu, X. Lei, and X. Tang, "Low ambiguity zone: Theoretical bounds and Doppler-resilient sequence design in integrated sensing and communication systems," *IEEE J. Sel. Areas Commun.*, vol. 40, no. 6, pp. 1809–1822, Jun. 2022.

[36] B. M. Popovic, "Optimum sets of interference-free sequences with zero autocorrelation zones," *IEEE Trans. Inf. Theory*, vol. 64, no. 4, pp. 2876–2882, Apr. 2018.

[37] M. H. AlSharif, M. Saad, M. Siala, T. Ballal, H. Boujemaa, and T. Y. Al-Naffouri, "Zadoff-chu coded ultrasonic signal for accurate range estimation," in *Proc. 25th Eur. Signal Process. Conf. (EUSIPCO)*, Kos island, Greece, Aug. 2017, pp. 1250–1254.

[38] Y. Zhou, H. Yin, N. Zhou, Y. Tang, X. Zhang, and W. Yuan, "GI-free pilot-aided channel estimation for affine frequency division multiplexing systems," 2024, *arXiv:2404.01088*.

Zhaocheng Wang (Fellow, IEEE) received the B.S., M.S., and Ph.D. degrees from Tsinghua University in 1991, 1993, and 1996, respectively.

Since 2009, he has been a Professor with the Department of Electronic Engineering, Tsinghua University, where he is currently the Director of the Broadband Communication Key Laboratory, Beijing National Research Center for Information Science and Technology (BNRist). He has authored or co-authored two books, which have been selected by *IEEE Press Series on Digital and Mobile Communications* (Wiley-IEEE Press). He has also authored/co-authored more than 160 peer-reviewed journal articles. He holds 46 U.S./EU granted patents (23 of them as the first inventor). His research interests include wireless communications, millimeter wave communications, and optical wireless communications. He is a fellow of the Institution of Engineering and Technology. He was a recipient of the ICC2013 Best Paper Award, the OECC2015 Best Student Paper Award, the 2016 IEEE Scott Helt Memorial Award, the 2016 IET Premium Award, the 2016 National Award for Science and Technology Progress (First Prize), the ICC2017 Best Paper Award, the 2018 IEEE ComSoc Asia–Pacific Outstanding Paper Award, and the 2020 IEEE ComSoc Leonard G. Abraham Prize. He was an Associate Editor of IEEE TRANSACTIONS ON WIRELESS COMMUNICATIONS from 2011 to 2015 and IEEE COMMUNICATIONS LETTERS from 2013 to 2016. He is an Associate Editor of IEEE TRANSACTIONS ON COMMUNICATIONS, IEEE SYSTEMS JOURNAL, and IEEE OPEN JOURNAL OF VEHICULAR TECHNOLOGY.

Tianqi Mao (Member, IEEE) received the B.S., M.S. (Hons.), and Ph.D. (Hons.) degrees from Tsinghua University in 2015, 2018, and January 2022, respectively. He is currently an Associate Professor with the School of Interdisciplinary Science, Beijing Institute of Technology, Beijing, China. He has authored over 60 journal and conference papers, including three Highly Cited Papers of ESI (as the first author). His research interests include modulation, waveform design, and signal processing for wireless communications, integrated sensing and communication, and AI/LLM-enabled communications. He was a recipient of the Young Elite Scientists Sponsorship Program by China Association for Science and Technology, the Science and Technology Award (Second Prize) of China Institute of Communications, and the Outstanding Ph.D. Graduate of Beijing City. He was the winner of the IEEE IWCMC 2024 Best Paper Award and the IEEE GLOBECOM 2023 Best Workshop Paper Award. He was the Lead Workshop Chair of IEEE PIMRC 2025, the Organizer of an industry panel at IEEE WCNC 2024, and a Tutorial Lecturer of IEEE ICC 2025, IEEE VTC-Fall 2024, and IEEE IWCMC 2024. He was the Lead Guest Editor of *IEEE Network*, a Guest Editor of IEEE TRANSACTIONS ON MOLECULAR, BIOLOGICAL, AND MULTI-SCALE COMMUNICATIONS and IEEE OPEN JOURNAL OF THE COMMUNICATIONS SOCIETY (two Special Issues). He is an Associate Editor of IEEE TRANSACTIONS ON COMMUNICATIONS, IEEE TRANSACTIONS ON VEHICULAR TECHNOLOGY, IEEE COMMUNICATIONS LETTERS, and IEEE OPEN JOURNAL OF VEHICULAR TECHNOLOGY.

Fan Zhang (Student Member, IEEE) received the B.S. degree (Hons.) from the Department of Electronic Engineering, Tsinghua University, Beijing, China, in 2022, where she is currently pursuing the Ph.D. degree. Her main research interests include wireless communications, signal processing, and waveform design in joint sensing and communication systems. She was a recipient of the IEEE IWCMC 2024 Best Paper Award, the National Scholarship, and the Outstanding B.S. Graduate of Beijing City.

Tianyu Jiao is currently pursuing the B.E. degree with the Department of Electronic Engineering, Tsinghua University, Beijing, China. His main research interests include machine learning and signal processing.

Yinxiao Zhuo received the B.S. and Ph.D. degrees from Tsinghua University in 2020 and 2025, respectively. His current research interests include mmWave communications and multi-beam integrated sensing and communication.

Miaowen Wen (Senior Member, IEEE) received the Ph.D. degree in signal and information processing from Peking University. He is currently a Professor with South China University of Technology, Guangzhou, China. He has authored or co-authored two books and more than 270 journal articles. His research interests include a variety of topics in the areas of wireless and molecular communications. He is serving as an Editor/Senior Editor for IEEE TRANSACTIONS ON WIRELESS COMMUNICATIONS, IEEE TRANSACTIONS ON MOLECULAR, BIOLOGICAL, AND MULTI-SCALE COMMUNICATIONS, and IEEE COMMUNICATIONS LETTERS. He served as an Editor for IEEE TRANSACTIONS ON COMMUNICATIONS from 2019 to 2024.

Wei Xiang (Senior Member, IEEE) is currently the Cisco Research Chair of AI and the Internet of Things (IoT) and the Director of the Cisco-La Trobe Centre for AI and the IoT and La Trobe University. He has published over 300 peer-reviewed papers, including three books and 220 journal articles. His research interests include the IoT, wireless communications, machine learning for the IoT data analytics, and computer vision. Due to his instrumental leadership in establishing Australia's first accredited Internet of Things Engineering Degree Program, he was inducted into the Pearcy Foundation's Hall of Fame in October 2018. He was named a Queensland International Fellow by Queensland Government of Australia from 2010 to 2011, an Endeavour Research Fellow by the Commonwealth Government of Australia from 2012 to 2013, a Smart Futures Fellow by Queensland Government of Australia from 2012 to 2015, and a JSPS Invitational Fellow jointly by Australian Academy of Science and Japanese Society for Promotion of Science from 2014 to 2015. He received the TNQ Innovation Award in 2016, the Pearcey Entrepreneurship Award in 2017, and the Engineers Australia Cairns Engineer of the Year in 2017. He has been awarded several prestigious fellowship titles. He was a co-recipient of four Best Paper Awards at WiSATS'2019, WCSP'2015, IEEE WCNC'2011, and ICWMC'2009. He has served in a large number of international conferences in the capacity of the general co-chair, the TPC co-chair, and the symposium chair. He was the Vice Chair of the IEEE Northern Australia Section from 2016 to 2020. He is an Associate Editor of IEEE COMMUNICATIONS SURVEYS AND TUTORIALS, IEEE TRANSACTIONS ON VEHICULAR TECHNOLOGY, IEEE INTERNET OF THINGS JOURNAL, IEEE ACCESS, and *Scientific Reports* (Nature). He is a TEDx Speaker and an Elected Fellow of IET in U.K., and Engineers Australia.

Sheng Chen (Life Fellow, IEEE) received the B.Eng. degree in control engineering from East China Petroleum Institute, Dongying, China, in January 1982, the Ph.D. degree in control engineering from City University, London, in September 1986, and the D.Sc. degree from the University of Southampton, Southampton, U.K., in August 2005. From 1986 to 1999, he held research and academic appointments at The University of Sheffield, Edinburgh, U.K., and in Portsmouth, U.K. Since 1999, he has been with the School of Electronics and Computer Science, University of Southampton, U.K., where he holds the post of a Professor of intelligent systems and signal processing. He was half-retired from the University of Southampton in 2023. Since 2023, he has been a Distinguished Professor with the School of Computer Science and Technology, Ocean University of China, Qingdao, China. He has published over 700 research articles. He has more than 21 000 Web of Science citations with an H-index of 64 and 41 000 Google Scholar citations with an H-index of 86. His research interests include adaptive signal processing, wireless communications, modeling and identification of nonlinear systems, neural networks, and machine learning. He is a fellow of United Kingdom Royal Academy of Engineering, a fellow of Asia–Pacific Artificial Intelligence Association, and a fellow of IET. He was one of the original 200 ISI highly cited researchers in engineering in March 2004.

George K. Karagiannidis (Fellow, IEEE) received the Ph.D. degree in telecommunications engineering from the Electrical Engineering Department, University of Patras, Greece, in 1998. He is currently a Professor with the Electrical and Computer Engineering Department, Aristotle University of Thessaloniki, Thessaloniki, Greece, and the Head of the Wireless Communications and Information Processing (WCIP) Group. His research interests include wireless communications systems and networks, signal processing, optical wireless communications, wireless power transfer, and signal processing for biomedical engineering. He recently received three prestigious awards: The 2021 IEEE ComSoc RCC Technical Recognition Award, the 2018 IEEE ComSoc SPCE Technical Recognition Award, and the 2022 Humboldt Research Award from the Alexander von Humboldt Foundation. He is one of the highly cited authors across all areas of electrical engineering, recognized by Clarivate Analytics as the Web of Science Highly Cited Researcher for the ten consecutive years 2015–2024. He was the Editor-in-Chief of IEEE COMMUNICATIONS LETTERS. He is the Editor-in-Chief of IEEE TRANSACTIONS ON COMMUNICATIONS.